AD_____

Award Number: W81XWH-06-1-0389

TITLE: Contrast Enhancement for Thermal Acoustic Breast Cancer Imaging via Resonant Stimulation

PRINCIPAL INVESTIGATOR: Jian Li Ph.D.
Mark Sheplak Ph.D.
Lou Cattafesta Ph.D.
Henry Zmuda Ph.D.
Huabei Jiang Ph.D.
Manuel Arreola Ph.D.

CONTRACTING ORGANIZATION: University of Florida
Gainesville, FL 32603

REPORT DATE: March 2008

TYPE OF REPORT: Annual

PREPARED FOR: U.S. Army Medical Research and Materiel Command
Fort Detrick, Maryland 21702-5012

REPORT DOCUMENTATION PAGE

Form Approved
OMB No. 0704-0188

1. REPORT DATE *(DD-MM-YYYY)*	**2. REPORT TYPE**	**3. DATES COVERED** *(From - To)*
01-03-2008	Annual	27 Feb 2007 - 26 Feb 2008

4. TITLE AND SUBTITLE

Contrast Enhancement for Thermal Acoustic Breast Cancer Imaging via Resonant Stimulation

5a. CONTRACT NUMBER

5b. GRANT NUMBER
W81XWH-06-1-0389

5c. PROGRAM ELEMENT NUMBER

6. AUTHOR(S)
Jian Li Ph.D., Mark Sheplak Ph.D., Lou Cattafesta Ph.D., Henry Zmuda Ph.D., Huabei Jiang Ph.D., Manuel Arreola Ph.D.

E-Mail: li@dsp.ufl.edu

5d. PROJECT NUMBER

5e. TASK NUMBER

5f. WORK UNIT NUMBER

7. PERFORMING ORGANIZATION NAME(S) AND ADDRESS(ES)

University of Florida
Gainesville, FL 32603

8. PERFORMING ORGANIZATION REPORT NUMBER

9. SPONSORING / MONITORING AGENCY NAME(S) AND ADDRESS(ES)
U.S. Army Medical Research and Materiel Command
Fort Detrick, Maryland 21702-5012

10. SPONSOR/MONITOR'S ACRONYM(S)

11. SPONSOR/MONITOR'S REPORT NUMBER(S)

12. DISTRIBUTION / AVAILABILITY STATEMENT
Approved for Public Release; Distribution Unlimited

13. SUPPLEMENTARY NOTES

14. ABSTRACT

This research plans to develop enhanced contrast thermal acoustic imaging (TAI) technology for the detection of breast cancer by combining amplitude-modulated (AM) electromagnetic (EM) field excitation, resonant acoustic scattering, and advanced signal processing techniques. While EM-induced TAI possesses great promise, the thermal acoustic signals tend to be weak. However, when the tumor is excited into resonance via EM stimulation, the effective acoustic scattering cross-section may increase by a factor in excess of 100 based on predictions for microsphere-based ultrasound contrast agents. Such an increase would truly be revolutionary, making the EM-induced TAI technology a very promising candidate for routine breast screening. The image formation methods in the existing TAI systems are data-independent and have poor resolution and high sidelobe problems. We will devise adaptive image formation algorithms to achieve high resolution and excellent interference and noise suppression capability.

15. SUBJECT TERMS
Thermal Acoustic Imaging (TAI), Resonance, Electromagnetic, Adaptive Imaging

16. SECURITY CLASSIFICATION OF:			**17. LIMITATION OF ABSTRACT**	**18. NUMBER OF PAGES**	**19a. NAME OF RESPONSIBLE PERSON**
a. REPORT	**b. ABSTRACT**	**c. THIS PAGE**			USAMRMC
U	U	U	UU	30	**19b. TELEPHONE NUMBER** *(include area code)*

Table of Contents

I. Introduction

We are in the second year of a three year effort focused on developing enhanced contrast thermal acoustic imaging (TAI) technology for the detection of breast cancer by combining amplitude-modulated (AM) electromagnetic (EM) field excitation, resonant acoustic scattering, and advanced signal processing techniques. EM-induced TAI combines the merits of both EM stimulation and ultrasound imaging, while overcoming their respective limitations. EM imaging provides excellent contrast between cancerous and normal breast tissue, but the long wavelengths provide poor spatial resolution. Conventional ultrasound imaging possesses very fine millimeter-range spatial resolution but poor soft tissue contrast. While EM-induced TAI possesses great promise, the thermal acoustic signals tend to be weak. However, when the tumor is excited into resonance via EM stimulation, the effective acoustic scattering cross-section may increase by a factor in excess of 100 based on predictions for microsphere-based ultrasound contrast agents. Such an increase would truly be revolutionary, making the EM-induced TAI technology a very promising candidate for routine breast screening. To induce the resonant response from the tumor, we are considering various approaches including, for example, AM continuous wave (CW) EM stimulation, where the modulation frequency range contains the predicted resonant frequencies for a distribution of tumor sizes and contrast ratios. The carrier frequency of the EM stimulation can be fixed and chosen for the best penetration and heat absorption. The image formation methods in the existing TAI systems are predominantly data-independent delay-and-sum (with or without weighting) type of approaches. These approaches tend to have poor resolution (relative to the best possible resolution a transducer array can offer) and high sidelobe problems, especially when the transducer array is not composed of uniformly and linearly spaced transducers, which is the case for the existing TAI systems. We are devising adaptive image formation algorithms to achieve high resolution and excellent interference and noise suppression capability.

The research efforts this year were focused on the following areas: initial phantom resonance experiments, further development of tissue mimicking breast phantoms, electric field measurements, electrical-to-acoustical transduction, creating a 3-D electromagnetic stimulation system, and validating the effectiveness of the multifrequency adaptive and robust technique for image reconstruction.

II. Body

II. 1 Experimental Progress

(a) Initial Phantom Resonance Experiments

Experimentation designed to verify acoustic resonance of the tumor phantom by electromagnetic excitation is underway. The experiment setup, shown schematically in Figure 1, consists of an electromagnetic waveguide, two ultrasonic transducers (one for transmission ant the other for sensing), and a Plexiglas cylinder that contains the de-ionized water and tumor phantom. The cylinder height is 10.3 inches and the inner diameter is 7.25 inches. The transducer used in the experiment is a 0.5 inch diameter piezoelectric immersion transducer from Olympus NDT (model V303). It has a center

frequency of 0.91 MHz and 60.275%, -6 dB bandwidth. At 1 MHz, the half angle beamwidth is approximately 3.5°. Reciprocity calibrations are being performed in de-ionized water. The waveguide used is from Penn Engineering Components (model WR 187) with a frequency range of 3.95-5.85 GHz. In the ongoing experiments, a 1 cm diameter sample of the phantom is suspended in the center of the cylinder, submerged in de-ionized water, and aligned with the ultrasonic transducers. The transmitting transducer is mounted to the side of the cylinder with the transducer face exposed to the de-ionized water. The receiving transducer is similarly aligned and its axis makes a 180-degree with respect to the first transducer. The electromagnetic waveguide provides excitation from the bottom of the cylinder. Electric field probes are inserted through a port in the top of the cylinder and are used to measure total field intensity along the cylinder axis. Two probes are needed: one to measure the radial field intensity and another to determine the axial field strength. The radial field probe is shown in Figure 4. The goal of the preliminary setup is to achieve a uniform field within a 3 cm radius around the phantom. The frequency of the 434 MHz radio frequency signal can be amplitude modulated over a range on the order of 400 kHz to 4 MHz, which is the expected range the resonant frequency of the phantom. The acoustic signal from the phantom is measured by the ultrasonic transducer and is recorded by the NI data acquisition system.

Initially, the tumor's resonant frequency is established acoustically. Referring to Figure 1, a swept sinusoidal signal generated emanating from Port 1 of an RF network analyzer acts as a source which drives one acoustic transducer while the second acoustic transducer, used to receive the acoustic signal, drives port 2.With the tumor absent from the water-filled tank, the received signal consists of the acoustic frequency characteristics of the tank itself, and this frequency response is used as a reference to calibrate the network analyzer. The same sweep is then performed with the tumor phantom present and the response now contains the resonant characteristics of the phantom. A typical frequency response is shown in Figure 2 where it is seen that the resonant frequency occurs between around 1 MHz.

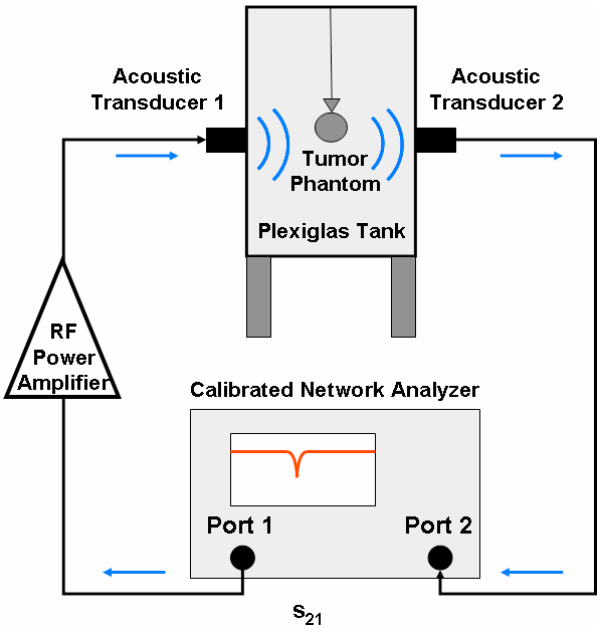

Figure 1: Test setup for determining the resonant frequency of the tumor phantom.

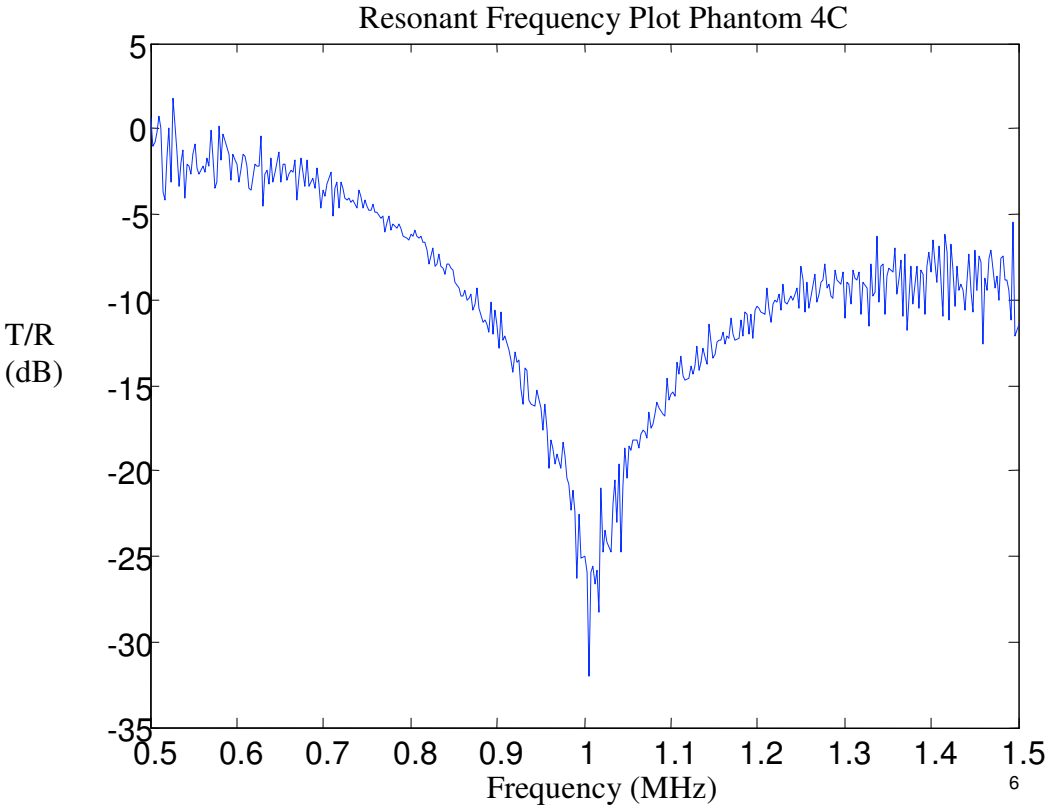

Figure 2: A typical frequency response of acoustic resonance.

For TAI systems the acoustic pressure wave is generated as the tumor is heated via application of EM energy. Having established the resonant frequency of the phantom using the acoustic technique described, a signal with this frequency amplitude modulated at 434 MHz EM carrier signal is then used to drive the waveguide located at the bottom of the tank via an RF power amplifier. The acoustic transducer is then used to sense the acoustic pressure wave generated by the TAI process.

(b) Phantom Aging Characteristics

While carrying out these measurements, it became apparent the large number of variables involved in characterizing the resonance of the phantom, one being the affect of aging of the phantom over time. Subsequently, some time was focused to characterize the phantom aging. One of the aspects explored was the variation of the resonant frequency over time. Figure 3 shows results based on the experimental setup described in the previous section and shown in Figure 1. While the sample size consists of only 3 phantoms, the general trend seems to be that the resonant frequency initially increases before it decreases over time. More specimens need to be studied to confirm this trend. In Figure 3, phantom c exhibited no apparent resonance in week one. This was attributed

to phantom placement in the cylinder. The setup was consequently altered in a way that would insure repeatable phantom placement. Phantom aging is important to quantify in order to minimize experimental error over time. Other properties are currently being examined including density and speed of sound.

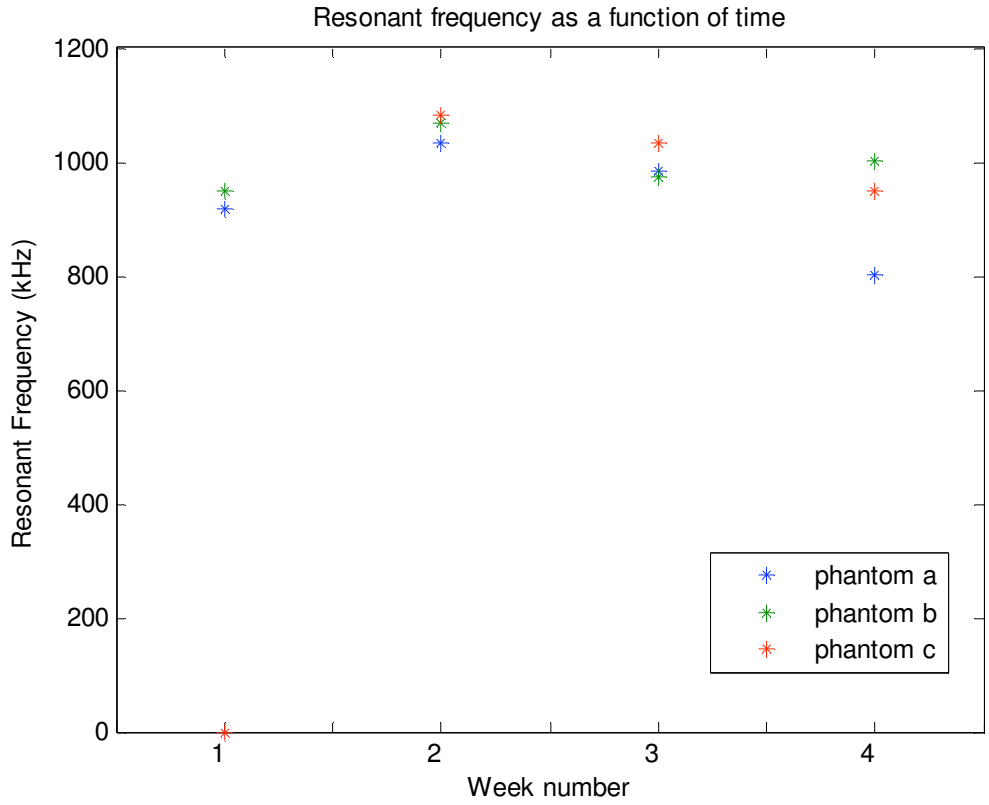

Figure 3: Resonant frequency of phantom over time. Note no resonance was found for phantom c in the first week.

(c) Electric Field Measurements

Accurate modeling of both the acoustical and electrical behavior of the system forms an essential component of this research effort. Of special concern is the ability to model electrical-to-acoustical transduction aspect of this system. The acoustic pressure wave to be measured is generated when the modulated electrical signal heats the phantom causing it to mechanically undulate. This heating occurs as a result of the electric field intensity in the location of the conducting phantom. As a consequence not only must the electrical fields present in this system be accurately modeled, but these fields must also be verified so that the proper heating parameters may be used as input to the acoustic model. Initially an off-the-shelf, low-profile, high-resolution probe that measures the electric potential (Carsten Associates Model E-601) was used. Once the potential is known a differencing procedure can be used to determine the field. It was found, however, that this method proved inadequate for the present system. In particular, the common mode signal measured far outweighed the difference signal and an accurate estimate of the electric field could not be determined. Further, the metal shaft of the probe, though small in diameter, was distorting the field in the tank. To remedy these, two custom

probes, one used to measure the axial field, another used to measure the radial field were designed. Since the new probes measure the electric field directly no differencing is required. Furthermore the new probes are design with a shaft that is impedance-matched to the impedance of de-ionized water thus making the probe transparent except of course (unavoidably) for the immediate region being measured. To date the radial field probe has been obtained and is shown in Figure 4. Shown also in Figure 4 is a Transverse Electro-Magnetic (TEM) test cell used for probe calibration. One end of the TEM cell is excited with a 434 MHz signal while the other end is terminated in a 50-ohm load. Since the dimensions of the cell are precisely known, the electric field in the cell's center is also known. This center portion of the TEM cell is filled with de-ionized water in which the probe is inserted, and the resulting voltage is measured using a 50-ohm oscilloscope. Once the axial filed probe is completed, an accurate field map of the tank along the axis where the phantom will be placed will be obtained. Once again this data will be used to verify the electromagnetic model and link the electrical and acoustic models.

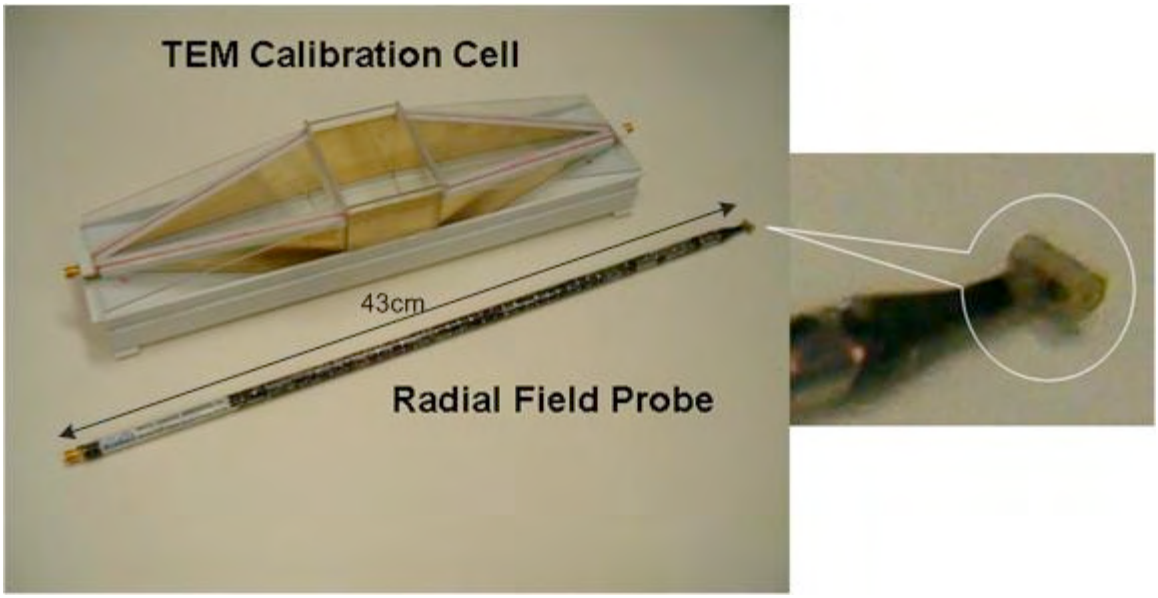

Figure 4: Radial field probe and probe calibration cell.

(d) Electrical-to-Acoustical Transduction

To date two problems have been encountered with regard to accurately measuring the RTAI effect and are currently being remedied. The first regards drift of the acoustic-acoustic resonance measurements. Since the acoustic transducers possess narrow beamwidths, accurate placement of the phantom is required for a stable resonance. Secondly the acoustic resonance varies with the temperature of the water. Initially the acoustic and electrical portions of the experimental procedure where performed consecutively. It has been determined that monitoring the acoustic resonance while the electrical measurements are taken is essential. Furthermore, to date the electrical (RF) power level has been kept low with a total drive power of less than four watts. This requires that the measurement bandwidth be kept small so as to not allow excessive noise

in the measurements. A new RF power amplifier capable of producing a drive power of up to 100-watts has been obtained. This, along with accurate placement of the phantom's location will allow for a robust, stable measurement of the RTAI effect.

II. 2 Electromagnetic Stimulation

Use of the RTAI concept as a real imaging application requires extending the approach to a three-dimensional system. As the experimental portion of present phase of the research effort continues so does the modeling for the next phase of the effort which involves three-dimensional modeling, simulation, and measurements.

Figure 5 illustrates conceptually how the required uniform electric field for a realistic breast phantom can be achieved in a simple and practical manner. Consider the situation shown in Figure 5(a) which illustrates a dielectric sphere of arbitrary permittivity in free space. It is well known in electromagnetic theory that a sinusoidally-distributed surface charge distribution, $\rho_S = \rho_o \cos\theta$, with ρ_o as a constant, placed on the surface of the sphere results in a perfectly uniform electric field inside the dielectric sphere as shown. By invoking the theory of images a Perfect Magnetic Conductor (PMC), which represents a good model for the chest wall, can be placed as shown without altering the electric field in the sphere. In this way a uniform electric field in a hemispherical region that models the human breast can be obtained. Obtaining such a surface charge distribution is, in general not possible, though it can be approximated in a pointwise fashion as illustrated in Figure 5(b). There it is seen that small (subresonant) patches can be placed on the breast so as to approximate a uniform electric field inside the breast. These (metal) patches would be coated with a non-conducting material and hence modeled as capacitively coupled as shown. The concept is akin to the approach used to obtain a uniform, circularly polarized transverse magnetic field from discrete wire cage structure in Magnetic Resonance Imaging (MRI) applications. Though the perfectly uniform field would be obtained only for the case of an electrostatic charge distribution, it is not unreasonable to expect a quasi-static solution which reasonably approximates the ideal, static situation under appropriate conditions, and this is currently being explored.

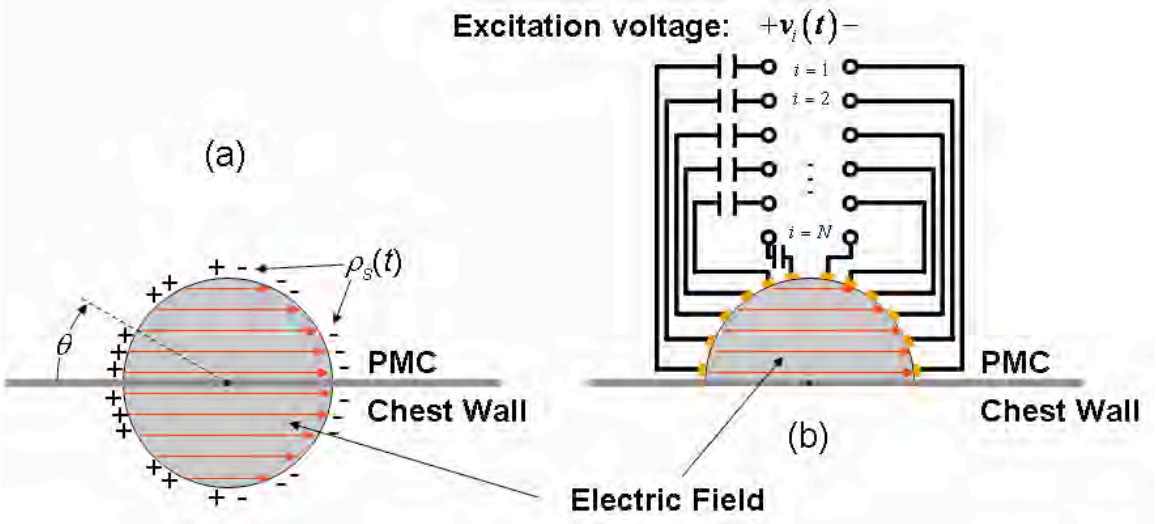

Figure 5: Motivation for achieving a uniform field within a hemispherical region using small, capacitively coupled patches.

To illustrate the basic idea, Figure 6 shows a pointwise electrostatic approximation to the continuous case using 31 point charges uniformly distributed over the breast phantom surface as indicated in Figure 6(b). The magnitudes of the point charges are chosen so that they equal the value of the continuous charge distribution at that point. This would serve, for example, as a good initial guess for a numerical optimization procedure which would give the optimum charge distribution that provide the most uniform electric field magnitude in the breast. Figure 6(c) shows the (unoptimized) electrostatic field intensity over several planes in the region to be imaged. It is seen that even for this simple case that the field intensity varies by less than 1 dB in the central region to be imaged. This approach is currently being developed analytically as well as being modeled using two commercially available software packages.

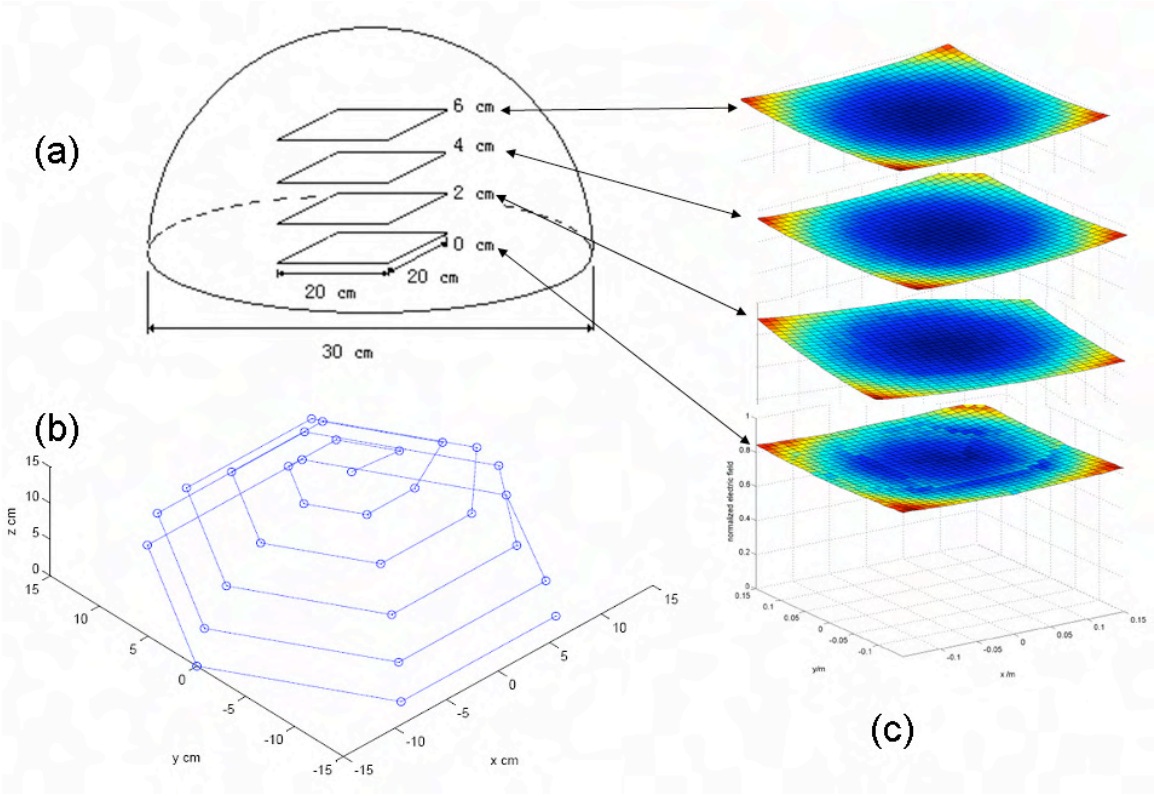

Figure 6: Simulated uniform electric field (quasi TEM) for a hemispherical shell excited by small patches.

II. 3 Adaptive Image Formation Algorithms

One of the key challenges encountered by thermal acoustic imaging (TAI) is to develop accurate and robust image reconstruction methods. Delay-and-sum (DAS) beamforming is a widely used reconstruction algorithm for TAI. However, this data independent approach tends to suffer from poor resolution and high sidelobe level problems. On the other hand, data adaptive approaches, such as the recently introduced

robust Capon beamforming (RCB) [1] method, can have much better resolution and much better interference rejection capabilities than their data independent counterpart.

We propose a multifrequency adaptive and robust technique (MART) based on RCB for TAI, where a multiple frequency source is employed instead of a single frequency source, which is generally used by other research groups. MART can offer higher signal-to-ratio (SNR) and higher imaging contrast than its single frequency counterpart, which we refer to as the single-frequency adaptive and robust technique (SART), since much more information about the human breast can be harvested from the multiple frequencies. Furthermore, the interference due to inhomogeneous breast tissue can be suppressed more effectively since more information about the breast tissue can be used by the RCB algorithm. MART is a three-stage time-domain signal processing algorithm. In Stage I, RCB is used to estimate the thermal acoustic responses from the focal points within the breast for each stimulating frequency. Then in Stage II, a scalar acoustic waveform at each focal point is estimated based on the response estimates for all frequencies from Stage I. Finally, in Stage III, the positive peak and the negative peak of the estimated acoustic waveform at each grid location are determined, and the peak-to-peak difference is computed and referred to as the image intensity.

To validate the effectiveness of the MART, we develop a 2-D inhomogeneous breast model, which includes skin, breast fatty tissues, glandular tissues, and the chest wall. Small tumors are set below the skin. The finite-difference time-domain (FDTD) method is used to simulate the electromagnetic field inside the breast tissues [2, 3]. The specific absorption rate (SAR) distribution is calculated based on the simulated electromagnetic field [4, 5]. Then FDTD is used again to simulate the propagation of the thermal acoustic waves [6, 7]. In the following example, the thermal acoustic signals are simulated based on the aforementioned 2-D model for multiple stimulating frequencies from 200-800 MHz with frequency step 100 MHz. Two small 1.5-mm-diameter tumors are set inside the breast model. Their locations are at (X=70 mm, Y=60 mm) and (X=75 mm, Y=62.5 mm). The distance between the two tumors is 4 mm. For comparison purposes, the DAS method is applied to the same data set. We also present the imaging results obtained by SART at different stimulating frequencies. Figure 7(a) and (b) show the imaging results for MART and DAS, respectively. The two tumors are seen clearly in the MART image, and the sizes and the locations of the two tumors are accurate. On the other hand, the DAS image contains much clutter and the two tumors cannot be separated clearly. Figure 7(c) and (d) show the imaging results for SART at the stimulating frequencies f=200 and 800 MHz, respectively. The tumors can be seen in both SART images, but more clutters show up in Figure 7(c) and (d) than in Figure 7(a), and the sizes of the two tumors in Figure 7(d) are larger than the true ones.

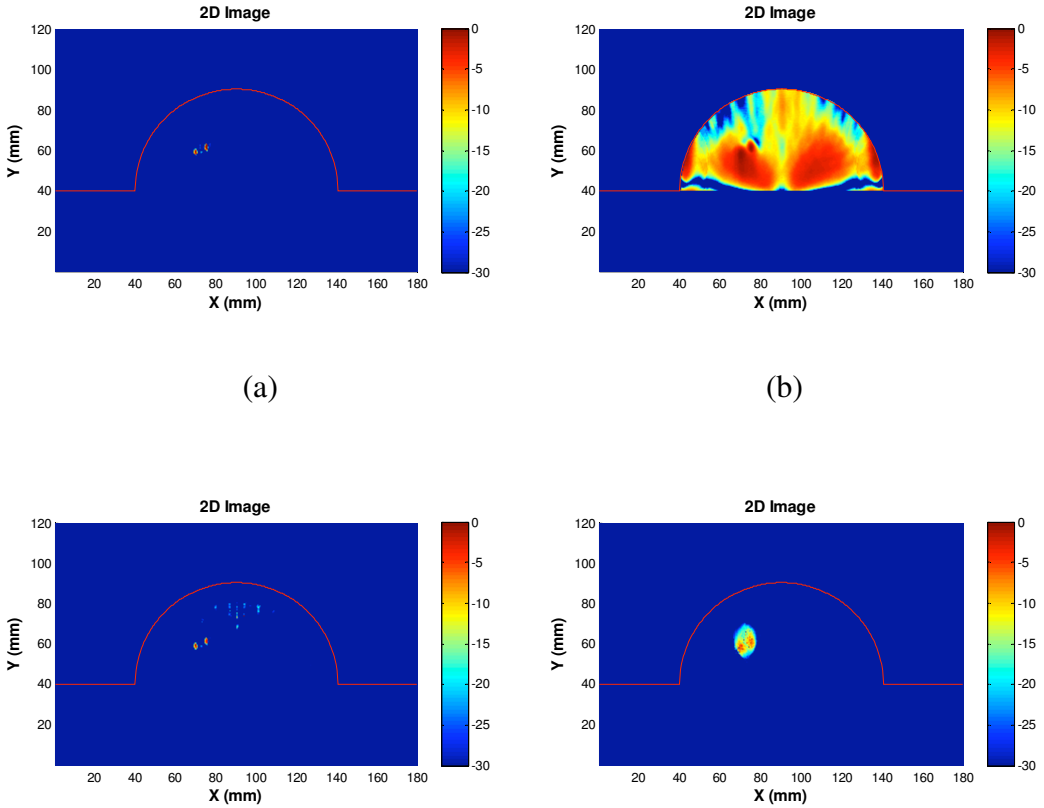

Figure 7: Reconstructed images obtained via (a) MART, (b) DAS, (c) SART at stimulating frequency f=200 MHz, (d) SART at stimulating frequency f=800 MHz.

III. Key Research Accomplishments

Phantom development was continued and properties as a function of aging were explored

Equipment needed for RF excitation and electric field measurements was identified and purchased (please see Table 1 for details)

Experimental setup to detect the thermal acoustic waves from the simulated tumor was formulated

A 3-D electromagnetic stimulation system is being simulated and developed

A 2-D inhomogeneous breast model, which includes skin, breast fatty tissues, glandular tissues, and the chest wall, was developed to validate the effectiveness of the MART

Vendor	Model number	Equiment purchased	Qt.
National Instruments	779079-02	NI PXI-5671 RF Signal Generator	1
Bruce Carsten Assoc.	EFP 200R	Calibrated radial probe	1
	EFP 200A	Calibrated axial probe	1
Mini-Circuits	ZHL-100W-52-S	Broadband Amplifier	1
Acopian	W530MT13	Power supply	1

Table 1: Equipment purchased this year.

IV. Reportable Outcomes

B. Guo, J. Li, H. Zmuda, and M. Sheplak, "Multi-Frequency Microwave Induced Thermal Acoustic Imaging for Breast Cancer Detection," IEEE Transactions on Biomedical Engineering, Vol. 54, No. 11, pp. 2000-2010, November 2007.

Y. Xie, B. Guo, J. Li, G. Ku, and L.V. Wang, "Adaptive and Robust Techniques (ART) for Thermoacoustic Tomography," to appear in IEEE Transactions on Biomedical Engineering.

V. Conclusion

Preliminary experiments were conducted to verify the feasibility of sensing the acoustic pressure from a tissue phantom excited at resonance. A tissue phantom that mimics the electrical and mechanical properties of a tumor for use in the excitation system has been designed. The preliminary phantom development focuses on matching dielectric properties, specifically permittivity and conductivity. The phantom was made from TX-151 powder (from Oil Research Center), water, cane sugar and potassium chloride. An iterative process of measuring the dielectric constants and manipulating the cane sugar and potassium chloride concentration was conducted until a suitable phantom was created.

The initial experiment has been designed to verify acoustic resonance of the tumor phantom by electromagnetic excitation. The experiment consists of an electromagnetic waveguide, a single ultrasonic transducer for sensing, and a Plexiglas cylinder that contains the deionized water and tumor phantom.

Currently the properties of the tumor phantom (dielectric constant, conductivity, and mechanical resonant frequency) are being evaluated as a function of temperature and time (age of the phantom). Preliminary results suggest that the positioning of the tumor phantom within the Plexiglas tank strongly influences measured results. These characteristics are being quantified so that repeatable results can be obtained. Since this proof-of-concept experimental setup uses only one acoustic transducer and one waveguide (EM) exciter, such sensitivity is not unexpected. The next generation system which uses multiple EM exciters and multiple acoustic receivers should reduce these sensitivities.

We have devised Adaptive and Robust Methods of Reconstruction (ARMOR) for thermoacoustic tomography. ARMOR is robust to the amplitude and phase distortions in the recorded signals caused by the acoustic heterogeneity of biological tissues. Examples based on a numerically simulated 2-D breast model and two sets of experimentally measured data from human mastectomy specimens demonstrate the excellent

performance of ARMOR: high resolution, low-side lobe level, and much improved interference suppression capability.

VI. References

[1] J. Li and P. Stoica, eds., *Robust Adaptive Beamforming*. New York, NY: John Wiley & Sons, 2005.

[2] A. Taflove and S. C. Hagness, *Computational Electrodynamics: The Finite-Difference Time-Domain Method*. Boston, MA: Artech House, second edition, 2000.

[3] D. M. Sullivan, *Electromagnetic Simulation Using the FDTD Method*. New York, NY: IEEE Press, 2000.

[4] P. Bernardi, M. Cavagnaro, S. Pisa, and E. Piuzzi, "Specific absorption rate and temperature elevation in a subject exposed in the far-fileld of radio-frequency sources operating in the 10-900-MHz range," *IEEE Transactions on Biomedical Engineering*, vol. 50, pp. 295-304, March 2003.

[5] P. Bernardi, M. Cavagnaro, S. Pisa, and E. Piuzzi, "SAR distribution and temperature increase in an anatomical model of the human eye exposed to the field radiated by the user antenna in a wireless LAN," *IEEE Transactions on Microwave Theory and Techniques*, vol. 46, pp. 2074-2082, December 1998.

[6] J. G. Maloney and K. E. Cummings, "Adaptation of FDTD techniques to acoustic modeling," *11th Annual Review of Progress in Applied Computational Electromagnetics, Monterey, CA*, vol. 2, pp. 724-731, 1995.

[7] X. Yuan, D. Borup, J. Wiskin, M. Berggren, and S. A. Johnson, "Simulation of acoustic wave propagation in dispersive media with relaxation losses by using FDTD method with PML absorbing boundary condition," *IEEE Transactions on Ultrasonics, Ferroelectrics, and Frequency Control*, vol. 46, pp. 14-23, January 1999.

VII. Appendices

"Multi-Frequency Microwave Induced Thermal Acoustic Imaging for Breast Cancer Detection"

"Adaptive and Robust Techniques (ART) for Thermoacoustic Tomography"

Multifrequency Microwave-Induced Thermal Acoustic Imaging for Breast Cancer Detection

Bin Guo, *Member, IEEE*, Jian Li*, *Fellow, IEEE*, Henry Zmuda, *Member, IEEE*, and Mark Sheplak

***Abstract*—Microwave-induced thermal acoustic imaging (TAI) is a promising early breast cancer detection technique, which combines the advantages of microwave stimulation and ultrasound imaging and offers a high imaging contrast, as well as high spatial resolution at the same time. A new multifrequency microwave-induced thermal acoustic imaging scheme for early breast cancer detection is proposed in this paper. Significantly more information about the human breast can be gathered using multiple frequency microwave stimulation. A multifrequency adaptive and robust technique (MART) is presented for image formation. Due to its data-adaptive nature, MART can achieve better resolution and better interference rejection capability than its data-independent counterparts, such as the delay-and-sum method. The effectiveness of this procedure is shown by several numerical examples based on 2-D breast models. The finite-difference time-domain method is used to simulate the electromagnetic field distribution, the absorbed microwave energy density, and the thermal acoustic field in the breast model.**

***Index Terms*—Breast cancer detection, finite-difference time-domain (FDTD) methods, multifrequency adaptive and robust technology (MART), robust capon beamforming (RCB), thermal acoustic imaging (TAI).**

I. Introduction

BREAST cancer is the most common nonskin malignancy in women and the second leading cause of female cancer mortality [1]. There are over 200 000 new cases of invasive breast cancer diagnosed each year in the U. S., and one out of every seven women in the U.S. will be diagnosed with breast cancer in their life time (the American Cancer Society, 2006) and early diagnosis is key to surviving breast cancer [2]. Microwave imaging is a method for early breast cancer detection [3]–[9], which exploits the significant contrast in dielectric properties between normal and cancerous tissues [10]–[12]. However, it is difficult for microwave imaging techniques to achieve good (submillimeter) spatial resolution because of its long wavelength [13]. Ultrasound is another option which offers a high spatial resolution because of its short acoustic wavelength [14]–[16]. However, the contrast in acoustic properties between normal and tumor tissues is very small due to both being soft tissues.

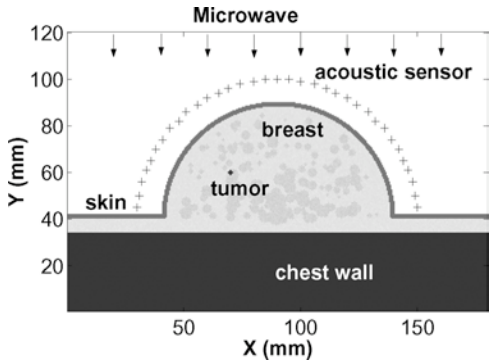

Fig. 1. Model of microwave-induced TAI for breast cancer detection.

Microwave-induced thermal acoustic imaging (TAI) combines the advantages of microwave stimulation and ultrasound imaging [13], which offers a high imaging contrast (due to the significantly different dielectric properties of tumor and normal breast tissues), as well as high spatial resolution (due to the low propagation velocity or the short wavelength of acoustic waves in biological tissues) at the same time. To use microwave-induced TAI techniques for breast cancer imaging, a microwave source with a short duration time is used to irradiate the breast, as shown in Fig. 1. The normal breast tissues, as well as tumors, absorb microwave energy and emanate thermal acoustic waves by thermoelastic expansion. It is well-known that malignant breast tissue has a higher water content [1], [10], [12], [17], with a much higher conductivity than normal breast tissues (with low water content). As a result, the microwave energy absorbed by tumor and normal breast tissues will be significantly different and a stronger acoustic wave will be produced by the tumor. The acoustic waves generated in this manner carry the information about the microwave energy absorption properties of the tissues under irradiation. The thermal acoustic waves propagate out of the breast and are recorded by an acoustic sensor array placed around the breast. The tumor locations can be accurately determined since the received acoustic signals from the malignant tumors are at higher levels, hence aiding image construction.

During the last decade, several research groups have been working on the microwave-induced TAI of biological tissues [18]–[23]. The microwave frequency used ranges from 400 MHz [22] to 3 GHz [13]. Image reconstruction algorithms include the

Manuscript received August 22, 2006; revised February 7, 2007. This work was supported in part by the National Institutes of Health under Grant 1R41CA107903-1, in part by the U.S. Army Medical Command under Contract W81XWH-06-1-0389, and in part by the National Natural Science Foundation of China under Grant 60428101. *Asterisk indicates corresponding author.*

B. Guo and H. Zmuda are with the Department of Electrical and Computer Engineering, University of Florida, Gainesville, FL 32611 USA (e-mail: guobin@dsp.ufl.edu).

*J. Li is with the Department of Electrical and Computer Engineering, P.O. Box 116130, University of Florida, Gainesville, FL 32611 USA (e-mail: li@dsp.ufl.edu).

M. Sheplak is with the Department of Mechanical and Aerospace Engineering, University of Florida, Gainesville, FL 32611 USA.

Color versions of one or more of the figures in this paper are available online at http://ieeexplore.ieee.org.

Digital Object Identifier 10.1109/TBME.2007.895108

widely used delay-and-sum (DAS) method [20], [23], the frequency-domain inverse method [24], [25], and the time-domain inverse method [13], [19].

Microwave-induced TAI does, however, present several challenges. First, the human breast is large in size, usually has an irregular shape if not compressed, and is covered with a 2–mm-thick skin with dielectric properties significantly different from the normal breast tissues. Moreover the breast tissue is far from homogeneous because the dielectric properties of glandular tissue are different from that of breast fatty tissue. All these factors make it difficult to approximate the back propagation properties of thermal acoustic signals inside the breast. Due to the slow acoustic wave propagation speed or short wavelength in biological tissues, the errors on the order of millimeters in determining the acoustic signal propagation path lengths will severely degrade the image quality.

In this paper, a multifrequency microwave-induced TAI system is proposed which remedy the problems mentioned above. Instead of using a single frequency microwave source, as generally done by other research groups in this field, here a multiple frequency source is used, since the desired thermal acoustic signals can be induced by microwave sources operating at a wide range of frequencies. We show in this paper that the rich information collected from the multifrequency stimulation can help mitigate the challenges mentioned. The multifrequency microwave-induced thermal acoustic signals will offer higher signal-to-noise ratio (SNR) and higher imaging contrast than single-frequency microwave-induced thermal acoustic signals since much more information about the human breast can be harvested from the multiple stimulating frequencies within the microwave frequency band. Furthermore, the interference due to inhomogeneous breast tissue can be suppressed more effectively when multifrequency microwave-induced thermal acoustic signals are used for image reconstruction since more information about breast tissue can be used by the adaptive image reconstruction algorithms.

Another challenge encountered by microwave-induced TAI is the need to develop accurate and robust image reconstruction methods. DAS is a widely used reconstruction algorithm in medical imaging. This method is data-independent and tends to suffer from poor resolution and high sidelobe level problems. Data-adaptive approaches, such as the recently introduced robust Capon beamforming (RCB) [26], [27] method, can have much better resolution and much better interference rejection capabilities than their data-independent counterpart. Several medical imaging algorithms [4], [5], [28], [29] based on RCB have been developed and used for microwave imaging and thermal acoustic imaging. Good performances of these algorithms have been reported.

We present a multifrequency adaptive and robust technique (MART) based on RCB for multifrequency microwave-induced TAI. There are three stages in our MART. In Stage I, RCB is used to estimate the thermal acoustic responses from the grid locations within the breast for each stimulating microwave frequency. Then, in Stage II, a scalar acoustic waveform at each grid location is estimated based on the response estimates for all stimulating frequencies from Stage I. Finally, in Stage III, the positive peak and the negative peak of the estimated acoustic waveform at each grid location are determined, and the peak-to-peak difference is computed and referred to as the image intensity.

To validate the effectiveness of the proposed algorithm, we develop a 2-D inhomogeneous breast model, which includes skin, breast fatty tissues, glandular tissues, and the chest wall. Small tumors are set below the skin. The finite-difference time-domain (FDTD) method is used to simulate the electromagnetic field inside the breast tissues [30], [31]. The specific absorption rate (SAR) distribution is calculated based on the simulated electromagnetic field [32], [33]. Then FDTD is used again to simulate the propagation of the microwave-induced thermal acoustic waves [34], [35].

The remainder of this paper is organized as follows. In Section II, the microwave frequency properties of human breast are described. A proper microwave frequency band for multifrequency microwave-induced TAI is also given in this section. MART is proposed for image formation in Section III. In Section IV, 2-D electromagnetic and acoustic breast models are developed. The electromagnetic and acoustic simulation methods are also presented in this section. Imaging results based on numerical examples are provided in Section V. Section VI concludes the paper.

II. Microwave Properties of Human Breast

A. Cutoff Frequency of Human Breast

In a microwave-induced TAI system, the biological tissues should be heated by microwave sources in a uniform manner, otherwise thermal acoustic signals will be induced by a nonuniform microwave energy distribution, resulting in images difficult to interrupt. It is well-known that high-order electromagnetic field modes will be excited in a media if the microwave works at a frequency higher than a cutoff frequency of the media [36], and the microwave energy distribution is nonuniform at high-order modes [37]. To minimize the nonuniform microwave energy distribution inside the breast caused by the high-order electromagnetic modes, the microwave source should work at a frequency below a certain cutoff frequency.

To estimate the cutoff frequency for the human breast, we consider the simplified breast model shown in Fig. 2(a) consisting of a semicircular dielectric waveguide with a perfect magnetic conductor (PMC) at the bottom of the semicircle. Recall that the tangential components of the magnetic field are zero on the surface at the PMC. The PMC assumption is reasonable because the permittivity of the chest wall ($\varepsilon_r = 50$) is much greater than that of the normal breast tissues ($\varepsilon_r = 9$). In circular dielectric waveguide, if an electromagnetic mode has a field distribution whose tangential magnetic field components are zero at the center line of the circular waveguide, as shown in Fig. 2(b), the introduction of a PMC at the center line of the circular waveguide will not significantly change the boundary conditions and, hence, will not significantly alter the mode distribution. The modes in the semicircular dielectric waveguide can, thus, be estimated by determining the modes in a corresponding circular dielectric waveguide.

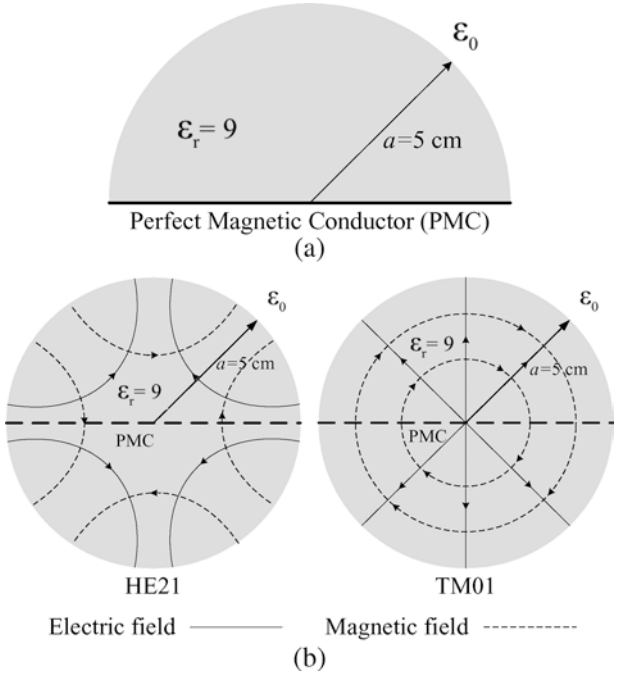

Fig. 2. Simplified breast model. (a) Semicircular dielectric waveguide with PEC, and (b) corresponding circular dielectric waveguide.

The dominant mode of a circular dielectric waveguide is the HE11 mode, the cutoff frequency of which is zero. The electromagnetic field distribution is near uniform at this mode. The dominant mode is followed by the TE01, TM01, and HE21 modes. These modes are degenerate, and have a cutoff frequency given by [36]

$$f_c = \frac{\chi_{01} C_0}{2\pi a \sqrt{\varepsilon_r - 1}} \tag{1}$$

where C_0 is the speed of light in free space, $\chi_{01} = 2.405$ is the first root of the Bessel function of the first kind of order zero $(J_0(\chi_{01}) = 0)$, a and ε_r are the radius and average permittivity of the circular dielectric waveguide, respectively. TM01 and HE21, as well as the interference between them, satisfy the zero tangential magnetic field component condition at the center line of the circular waveguide. These modes can also exist in the semicircular dielectric waveguide. By substituting the parameters of the breast model into (1), we obtain the cutoff frequency of the semicircular breast model to be

$$f_c = \frac{2.405 \cdot 3 \times 10^8}{2\pi \cdot 0.05 \cdot \sqrt{9-1}} = 812 \text{ MHz} \tag{2}$$

where we have used $a = 5$ cm and $\varepsilon_r = 9$ as typical values for human breast. Consequently, the stimulating microwave frequency for the TAI system should be below 812 MHz.

B. Microwave Energy Absorption Properties of Breast Tissues and Tumor

It is well-known that the complex relative dielectric properties of a medium can be expressed as

$$\varepsilon_r = \varepsilon_r' - j\varepsilon_r'' \tag{3}$$

TABLE I
COLE–COLE PARAMETERS FOR BIOLOGICAL TISSUES

Tissue	Breast	Skin	Muscle	Tumor
ε_∞	2.5	4.0	4.0	4.0
σ	0.01	0.0002	0.2	0.7
$\triangle\varepsilon_1$	3.0	32.0	50.0	50.0
τ_1 (ps)	17.68	7.23	7.23	7.0
α_1	0.1	0.0	0.1	0.0
$\triangle\varepsilon_2$	15	1100	7000	0
τ_2 (ns)	63.66	32.48	353.68	N/A
α_2	0.1	0.2	0.1	N/A
$\triangle\varepsilon_3$	5.0E4	0	1.2E6	0
τ_3 (μs)	454.7	N/A	318.31	N/A
α_3	0.1	N/A	0.1	N/A
$\triangle\varepsilon_4$	2.0E7	N/A	2.5E7	0
τ_4 (ms)	13.26	N/A	2.274	N/A
α_4	0.0	N/A	0.0	N/A

where ε_r' is the relative permittivity and ε_r'' is the out-of-phase loss factor which can be written as

$$\varepsilon_r'' = \frac{\sigma}{\varepsilon_0 \omega} \tag{4}$$

with σ being the total conductivity, ε_0 the free space permittivity, and ω the electromagnetic frequency. The tissue absorption property of the electromagnetic wave energy is

$$Q(\mathbf{r}) = \frac{1}{2}\sigma |E(\mathbf{r})|^2 \tag{5}$$

which is a function of the total conductivity and the electric field inside the tissue. If we assume that the microwave energy distribution is uniform inside the breast in a TAI system, the absorption of the microwave energy by the breast is characterized by the total conductivity of the breast tissues

$$\sigma(\omega) = \varepsilon_r'' \varepsilon_0 \omega. \tag{6}$$

Hence, instead of using the attenuation coefficient α, as used in [23], in this paper, we study the absorption properties of breast tissues using the total conductivity σ.

The dielectric properties of biological tissues can be accurately modeled by the Cole–Cole equation [38]

$$\varepsilon_r(\omega) = \varepsilon_\infty + \sum_{i=1}^{K} \frac{\Delta\varepsilon_i}{1 + (j\omega\tau_i)^{1-\alpha_i}} + \frac{\sigma_0}{j\omega\varepsilon_0} \tag{7}$$

where K is the order of the Cole–Cole model, ε_∞ is the high-frequency permittivity, τ_i is the relaxation time, $\Delta\varepsilon_i$ is the pole amplitude, α_i $(0 \le \alpha_i \le 1)$ is a measure of the broadening of dispersion, and σ_0 is the static ionic conductivity. The Cole–Cole parameters for skin, breast fatty tissue, chest wall (mainly consisting of muscle), as well as tumor are listed in Table I [39], [40]. Because we cannot find the values specific to the tumor, the dielectric properties of the tumor is approximated using a Debye model [3], [41], which is a special case of the Cole–Cole model.

Substituting (7) into (6), we obtain the total conductivity of the breast tissue as follows:

$$\sigma(\omega) = -\text{imag}\left(\varepsilon_\infty + \sum_{i=1}^{K} \frac{\Delta\varepsilon_i}{1 + (j\omega\tau_i)^{1-\alpha_i}} + \frac{\sigma}{j\omega\varepsilon_0}\right)\varepsilon_0\omega \tag{8}$$

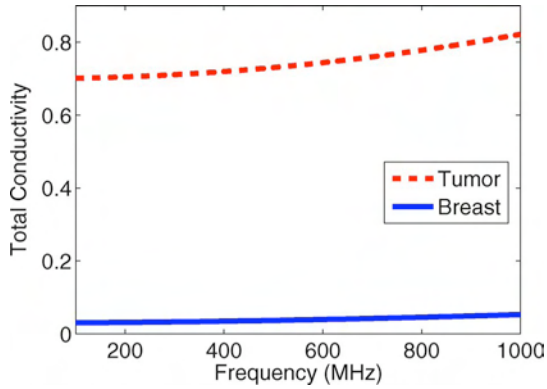

Fig. 3. Total conductivity of normal breast tissues and tumor as a function of frequency.

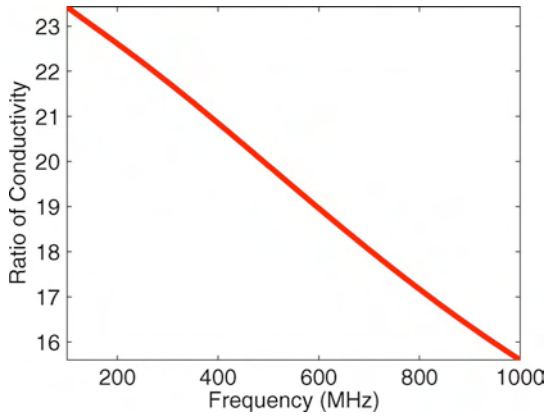

Fig. 4. Ratio of conductivity between tumor and normal breast tissue as a function of frequency.

which is a function of the stimulating microwave frequency, where $\mathrm{imag}(\cdot)$ denotes the imaginary part of the complex relative permittivity. Fig. 3 gives the total conductivity of breast fatty tissue and tumor over a frequency band from 100–1000 MHz. Note that the total conductivity increases with the microwave frequency, which means that more microwave energy is absorbed and converted to heat by tissues at higher microwave frequency region, or in other words, the SNR is higher in the received thermal acoustic signals at higher stimulating microwave frequency region. On the other hand, the penetration at higher microwave frequencies is smaller because the tissues are lossy. We define the conductivity ratio between the tumor and the normal breast tissue as

$$r_\sigma(\omega) = \frac{\sigma_{\mathrm{tumor}}(\omega)}{\sigma_{\mathrm{breast}}(\omega)} \tag{9}$$

and plot it as a function of frequency in Fig. 4. A high conductivity ratio means that more microwave energy is absorbed and converted to heat by tumor than by normal breast tissues. In other words, the higher the conductivity ratio, the higher the imaging contrast. Fig. 4 shows that the imaging contrast is higher at the lower microwave frequency region because the conductivity ratio decreases with the frequency.

These microwave energy absorption properties of breast tissues and tumor motivate us to consider inducing thermal acoustic signals with different microwave frequencies. By taking into account the aforementioned cutoff frequency given in (2), we choose a frequency range from 200–800 MHz. The frequency step is 100 MHz, with a total of seven frequencies. Note that wideband antenna techniques should be used for the practical implementation because the frequency range is wide. However, since the exciting microwave frequency is stepped, an antenna with a broad instantaneous bandwidth is not required. Another advantage of using multiple frequencies for stimulation is that more information about the inhomogeneous breast tissues will be harvested from the multifrequency microwave-induced thermal acoustic signals. The microwave energy distribution inside the breast model is not uniform because the human breast is inhomogeneous media, and thermal acoustic signals will be induced by the inhomogeneous energy distribution. These thermal acoustic signals will appear as clutter in the resulting images. However, the inhomogeneous microwave energy distributions are different at different stimulating frequencies because of the different microwave wavelengths in breast tissues. When a multifrequency microwave source is used for TAI, the thermal acoustic clutter induced by the inhomogeneous breast tissues can be suppressed by our adaptive and robust imaging algorithm.

III. Multifrequency Adaptive and Robust Technology (MART) for Breast Cancer Imaging

We consider a multifrequency microwave-induced TAI system as shown in Fig. 1, where an acoustic sensor array is arranged on a semicircle relatively close to the breast skin. The location of each acoustic sensor is $\mathbf{r}_j$ $(j = 1, \cdots, N)$, where N is the number of acoustic sensors. Assume that $M = 7$ microwave sources with different frequencies are used to irradiate the breast model. Let $p_{i,j}(t)$ $(i = 1, \cdots, M;\ j = 1, \cdots, N;\ t = 0, \cdots, T-1)$ denote the thermal acoustic signal induced by the i^{th} frequency and received by the j^{th} acoustic sensor, where T is the recording time which is sufficiently long to allow acoustic sensors to record all responses from the breast. Our goal is to detect the tumor by reconstructing an image of the thermal acoustic response intensity $I(\mathbf{r})$ as a function of scan location $\mathbf{r}$ within the breast.

A. Data Preprocessing

Because the breast skin, breast tissues, chest wall, and tumor absorb the microwave energy and convert the energy to heat, all of them produce thermal acoustic signals. The received thermal acoustic waveforms include the responses from the tumor, as well as from other healthy breast tissues. The thermal acoustic signals generated by the skin are much stronger than those by a small tumor because of the high conductivity of the skin and the acoustic sensors being very close to the skin. We must remove the skin responses to enhance the tumor responses. Because the distances between the acoustic sensors and the nearest breast skin are similar to one another, the signals recorded by various sensors have similar skin responses. Hence, we can remove the skin response by subtracting out a fixed calibration signal from all received signals. This calibration signal can be obtained simply by averaging the recorded signals from all channels.

Let $x_{i,j}(t)$ denote the signals after subtracting out the calibration signal. To process the signals coherently for a focal point

at $\mathbf{r}$, we align the signals $x_{i,j}(t)$ by time shifting each signal a number of samples $n_j(\mathbf{r})$. The discrete time delay between $\mathbf{r}$ and the j^{th} acoustic sensor can be calculated as

$$n_j(\mathbf{r}) = \left\lfloor \frac{\|\mathbf{r}_j - \mathbf{r}\|}{\Delta t c} \right\rceil \tag{10}$$

where $\lfloor \gamma \rceil$ stands for rounding to the greatest integer less than γ, $\|\mathbf{r}_j - \mathbf{r}\|$ is the distance between $\mathbf{r}_j$ and $\mathbf{r}$, c is the velocity of the acoustic wave propagating in breast tissues, and Δt is the sampling interval, which is assumed to be sufficiently small. The time-shifted signals are denoted as

$$\tilde{x}_{i,j}(t, \mathbf{r}) = x_{i,j}\left(t + n_j(\mathbf{r})\right), \quad t = -n_j(\mathbf{r}), \cdots, T - n_j(\mathbf{r}). \tag{11}$$

After time shifting, the acoustic signals from the imaging location $\mathbf{r}$ are aligned so that they all start approximately from time $t = 0$ for all channels. Now the aligned signals are windowed by

$$\text{Window}(l) = \begin{cases} 1, & 0 \le l \le L-1 \\ 0, & \text{otherwise} \end{cases} \tag{12}$$

to isolate the signals from the focal point at $\mathbf{r}$. The windowed signals are denoted as $\tilde{x}_{i,j}(l, \mathbf{r}), l = 0, \cdots, L-1$, where $L\Delta t$ is the approximate duration of the thermal acoustic pulse, which can be determined from the pulse duration of the pulsed microwave source.

Attenuation exists when acoustic waves propagate within the breast. This attenuation has two parts: the attenuation due to the lossy media and the propagation attenuation. Thus, the attenuation of the tumor responses at various channels are different because of the different distances between the imaging position $\mathbf{r}$ and the acoustic sensors. For the 2-D case considered here, the compensation factor for the j^{th} channel is given by

$$K_j(\mathbf{r}) = \exp\left(\alpha \|\mathbf{r}_j - \mathbf{r}\|\right) \cdot \|\mathbf{r}_j - \mathbf{r}\|^{1/2} \tag{13}$$

where the first term of the right side of (13) compensates for the attenuation due to the lossy media, and the second term compensates for the geometric attenuation. The compensated signal can be calculated as

$$y_{i,j}(l, \mathbf{r}) = K_j(\mathbf{r}) \cdot \tilde{x}_{i,j}(l, \mathbf{r}), \quad l = 0, \cdots, L-1. \tag{14}$$

B. Multifrequency Adaptive and Robust Technology (MART)

Without loss of generality, we consider imaging at a generic location $\mathbf{r}$ only. For notational convenience, we drop the dependence of $y_{i,j}(l, \mathbf{r})$ on $\mathbf{r}$, and simply denote it as $y_{i,j}(l)$. Now we consider the data model

$$y_{i,j}(l) = s_{i,j}(l) + e_{i,j}(l) \tag{15}$$

where $s_{i,j}(l)$ represents the tumor response and $e_{i,j}(l)$ represents the residual term, which includes the noise and interference from breast skin, chest wall, and other responses. The structure of the data model is a data cube as shown in Fig. 5.

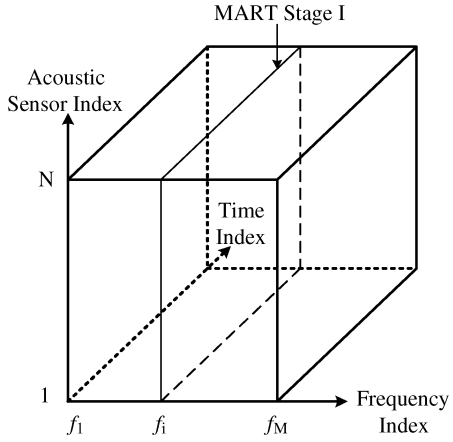

Fig. 5. Data cube model. In Stage I, MART slices the data cube for each frequency index. RCB is applied to each data slice to estimate the corresponding waveform.

MART is a three-stage time-domain signal processing algorithm. In Stage I, MART slices the data cube corresponding to each frequency index, and processes each data slice by the RCB to obtain the thermal acoustic waveform estimate for each stimulating frequency. Then, in Stage II, a scalar waveform is estimated from all frequencies based on the waveform estimates from Stage I. Finally, the positive peak and the negative peak of the estimated thermal acoustic waveform from Stage II are found in Stage III. The peak-to-peak difference is calculated as the image intensity at the focal point at $\mathbf{r}$. The details of all three stages are given below.

1) Stage I: In Stage I, MART approximates the data model as

$$\mathbf{y}_i(l) = \mathbf{a}_i s_i(l) + \mathbf{e}_i(l) \tag{16}$$

where $\mathbf{y}_i(l) = [y_{i,1}(l), \cdots, y_{i,N}(l)]^T$ and $\mathbf{e}_i(l) = [e_{i,1}(l), \cdots, e_{i,N}(l)]^T$. The scalar waveform $s_i(l)$ denotes the thermal acoustic signal generated at the focal location $\mathbf{r}$ corresponding to the i^{th} stimulating frequency. The vector $\mathbf{a}_i$ is referred to as the array steering vector, which is approximately equal to $\mathbf{1}_{N\times 1} = [1, \cdots, 1]^T$ since all the signals have been aligned temporally and their attenuation compensated for in the preprocessing step. The residual $\mathbf{e}_i(l)$ is the noise and interference term, which is assumed uncorrelated with the signal.

There are two assumptions made to write the model given in (16). First, the steering vector is assumed to vary with the microwave frequency (i) but nearly constant with the time sample (l). Second, we assume that the thermal acoustic signal waveform depends only on the microwave frequency (i) but not on the acoustic sensor (j). The truth, however, is that the steering vector is not exactly known as it changes slightly with both the stimulating frequency and time due to array calibration errors and other factors. The signal waveform can also vary slightly with both the stimulating frequency and acoustic sensor, due to the inhomogeneous and frequency-dependent medium within the breast. The two aforementioned assumptions simplify the problem slightly. They cause little performance degradations when used with our adaptive and robust algorithm.

In practice, the true steering vector in (16) is not $\mathbf{1}_{N\times 1}$. We assume that the true steering vector $\mathbf{a}_i$ lies in the vicinity of the assumed steering vector $\bar{\mathbf{a}} = \mathbf{1}_{N\times 1}$, and the only knowledge we have about $\mathbf{a}_i$ is that

$$\|\mathbf{a}_i - \bar{\mathbf{a}}\|^2 \leq \epsilon_1 \tag{17}$$

where ϵ_1 is a user parameter, which may be determined depending on the various errors discussed previously.

The true steering vector $\mathbf{a}_i$ can be estimated via the following covariance fitting approach of RCB [26], [27]

$$\max_{\delta_i^2, \mathbf{a}_i} \delta_i^2 \quad \text{subject to} \quad \hat{\mathbf{R}}_{\mathbf{Y}_i} - \delta_i^2 \mathbf{a}_i \mathbf{a}_i^T \geq 0 \qquad \|\mathbf{a}_i - \bar{\mathbf{a}}\|^2 \leq \epsilon_1 \tag{18}$$

where δ_i^2 is the power of the signal $s_i(l)$ and

$$\hat{\mathbf{R}}_{\mathbf{Y}_i} \triangleq \frac{1}{L} \sum_{l=0}^{L-1} \mathbf{y}_i(l) \mathbf{y}_i^T(l) \tag{19}$$

is the sample covariance matrix. The above optimization problem can be solved as described in [26], and the estimated true steering vector is denoted here as $\hat{\mathbf{a}}_i$.

To obtain the signal waveform estimate, we pass the received signals through a Capon beamformer [27], [42]. The weight vector of the beamformer is determined by using the estimated steering vector $\hat{\mathbf{a}}_i$ in the following expression:

$$\mathbf{w}_i = \frac{\hat{\mathbf{R}}_{\mathbf{Y}_i}^{-1} \hat{\mathbf{a}}_i}{\hat{\mathbf{a}}_i^T \hat{\mathbf{R}}_{\mathbf{Y}_i}^{-1} \hat{\mathbf{a}}_i}. \tag{20}$$

Then the estimated signal waveform corresponding to the i^{th} stimulating frequency is

$$\hat{s}_i(l) = \mathbf{w}_i^T \mathbf{y}_i(l). \tag{21}$$

By repeating the aforementioned process for $i = 1$ through $i = M$, we obtain the complete set of M waveform estimates

$$\hat{\mathbf{s}}(l) = [\hat{s}_1(l), \cdots, \hat{s}_M(l)]^T. \tag{22}$$

2) Stage II: Since the stimulating microwave sources with various frequencies are assumed to have the same power, we assume that the thermal acoustic responses from the tumor at different stimulating frequencies have nearly identical waveforms. Note that the thermal acoustic responses induced by the inhomogeneous microwave energy distribution (due to the inhomogeneous breast tissues) are different at different stimulating frequencies. This means that the elements of the vector $\hat{\mathbf{s}}(l)$ are all approximately equal to an unknown scalar signal $s(l)$, and the noise and interference term can be assumed uncorrelated with this signal. In Stage II of MART, we adopt the data model

$$\hat{\mathbf{s}}(l) = \mathbf{a}_s s(l) + \mathbf{e}_s(l) \tag{23}$$

where $\mathbf{a}_s$ is approximately equal to $\mathbf{1}_{M\times 1}$. However, the "steering vector" may again be imprecise, and, hence, RCB is needed again.

As we did in Stage I, we assume that the only knowledge about $\mathbf{a}_s$ is that

$$\|\mathbf{a}_s - \bar{\mathbf{a}}_s\|^2 \leq \epsilon_2, \tag{24}$$

where $\bar{\mathbf{a}}_s = \mathbf{1}_{M\times 1}$ is the assumed steering vector, and ϵ_2 is a user parameter. Again, the true steering vector $\mathbf{a}_s$ can be estimated via the covariance fitting approach

$$\max_{\delta^2, \mathbf{a}_s} \delta^2 \quad \text{subject to} \quad \hat{\mathbf{R}}_s - \delta^2 \mathbf{a}_s \mathbf{a}_s^T \geq 0 \qquad \|\mathbf{a}_s - \bar{\mathbf{a}}_s\|^2 \leq \epsilon_2 \tag{25}$$

where δ^2 is the power of the signal $s(l)$, and

$$\hat{\mathbf{R}}_s \triangleq \frac{1}{L} \sum_{l=0}^{L-1} \hat{\mathbf{s}}(l) \hat{\mathbf{s}}^T(l) \tag{26}$$

is the sample covariance matrix.

After obtaining the estimated steering vector $\hat{\mathbf{a}}_s$, we obtain the adaptive weight vector and the estimated signal waveform, respectively, as

$$\mathbf{w} = \frac{\hat{\mathbf{R}}_s^{-1} \hat{\mathbf{a}}_s}{\hat{\mathbf{a}}_s^T \hat{\mathbf{R}}_s^{-1} \hat{\mathbf{a}}_s} \tag{27}$$

and

$$\hat{s}(t) = \mathbf{w}^T \hat{\mathbf{s}}(t). \tag{28}$$

3) Stage III: Because the thermal acoustic pulse is usually bipolar: a positive peak, corresponding to the compression pulse, and a negative peak, corresponding to the rarefaction pulse [43], we use the peak-to-peak difference as the response intensity for the imaging location $\mathbf{r}$ in the third stage of MART. Compared with other energy or amplitude based response intensity estimation methods, peak-to-peak difference can be used to improve imaging quality with little additional computation costs.

The positive and negative peak values of the estimated waveform for the focal location $\mathbf{r}$ will be searched based on the estimated waveform (28) obtained in Stage II. Because of the nonuniform sound speed in biological tissues, the arrival time of the acoustic pulse generated at location $\mathbf{r}$ cannot be calculated accurately. However, it was reported in [18] that, when the heterogeneity is weak, such as in breast tissues, amplitude distortion caused by multipath is not severe. We assume that the original peak remains a peak in the estimated waveform, and the positive and negative peak values of the thermal acoustic pulse can be searched as

$$P^+ = \max \left\{ \max_{l \in [\Delta_1, \Delta_2]} \{\hat{s}(l)\}, 0 \right\} \tag{29}$$

and

$$P^- = \min \left\{ \min_{l \in [\Delta_1, \Delta_2]} \{\hat{s}(l)\}, 0 \right\} \tag{30}$$

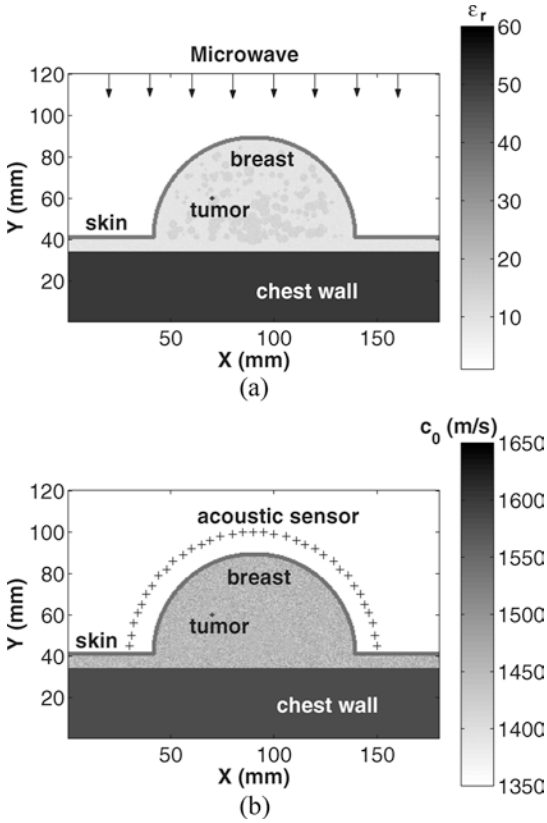

Fig. 6. Breast model for thermal acoustic simulation. (a) Model for electromagnetic simulation and (b) model for acoustic simulation.

where $[\Delta_1, \Delta_2] \in [0, L]$ is the searching range. Here Δ_1 and Δ_2 are user parameters, and the details on how to choose them can be found in [29].

After the positive and negative peak values are found, the response intensity for the focal point at location $\mathbf{r}$ is given as

$$I(\mathbf{r}) = P^+ - P^-. \tag{31}$$

IV. Modeling and Simulations

We consider 2-D breast models simulated in two steps. In the first step, the electromagnetic field inside the breast model is simulated and the SAR distribution is calculated based on the simulated electromagnetic field. The second step is for the acoustic wave simulation, where the SAR distribution obtained in the first step is used as the acoustic pressure source through the thermal expansion coefficient. In both steps, the FDTD method is used for the simulation examples.

A. Electromagnetic Model and Simulation

For simulation purposes, the 2-D electromagnetic breast model used is as shown in Fig. 6(a). The breast model is a 10 cm in diameter semicircle, which includes the skin, breast fatty tissue, glandular tissues, and chest wall (muscle). A 1-mm-diameter tumor is embedded below the skin. The dielectric properties of the breast tissues as well as tumor at the

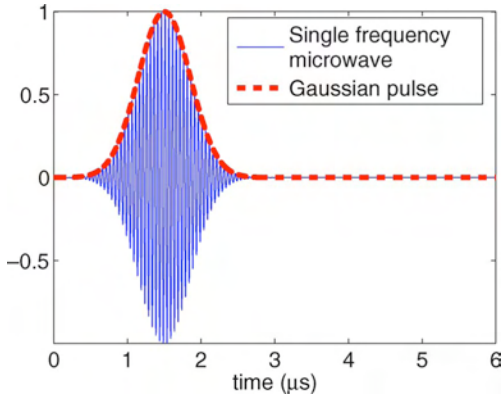

Fig. 7. Gaussian modulated microwave source.

microwave frequency f_i $(i = 1, \cdots, M)$ were calculated based on the Cole–Cole model in (7). The dielectric properties of the normal breast fatty tissue are assumed random with a variation of $\pm 10\%$ around the nominal values. The dielectric constants of glandular tissues are between $\varepsilon_r = 11$ and $\varepsilon_r = 15$.

Fig. 7 shows a Gaussian modulated electromagnetic wave used to irradiate the breast from the top of the model, as shown in Fig. 6(a). The time duration for the Gaussian pulse is 1 μs. The electromagnetic field is simulated using the FDTD method [30], [31]. The grid cell size used by FDTD is 0.5 × 0.5 mm and the computational region is terminated by perfectly matched layer (PML) absorbing boundary conditions [44], [45].

The SAR distribution is given as [32], [33]

$$\mathrm{SAR}(\mathbf{r}) = \frac{\sigma(\mathbf{r})E^2(\mathbf{r})}{2\rho(\mathbf{r})} \tag{32}$$

where $\sigma(\mathbf{r})$ is the conductivity of the biological tissues at location $\mathbf{r}$, $E(\mathbf{r})$ is the electric field at location $\mathbf{r}$, and $\rho(\mathbf{r})$ is the mass density of the biological tissues at location $\mathbf{r}$.

B. Acoustic Model and Simulation

In the microwave-induced TAI system, the microwave energy is small, and as a result, the acoustic pressure field induced by microwave is also small. So, the nonlinear acoustic effect does not need to be considered in the TAI system. For example, it is shown in [46] that the temperature rise is about 0.1 mK and the acoustic pressure change is only about 100 Pa in the microwave-induced TAI system. The shock distance in breast tissues is [47]

$$\chi_s = \frac{\frac{B}{2A}}{2\left(\frac{B}{2A}+1\right)} \cdot \frac{\rho_0 c^2}{p} \cdot \lambda_{\min} = \frac{\frac{B}{2A}}{2\left(\frac{B}{2A}+1\right)} \cdot \frac{\rho_0 c^2}{p} \cdot \frac{c}{f_{\max}} \tag{33}$$

where $(B/A)(\approx 10)$ is the nonlinear factor of the breast tissues, $\rho_0(\approx 1000\ \mathrm{kg/m^3})$ is the mass density of the breast tissues, and $c(\approx 1500\ \mathrm{m/s})$ is the sound speed inside the breast tissues [14]. p is the acoustic pressure rise, and $\lambda_{\min}$ and $f_{\max}$ are the minimal acoustic wavelength and the maximal acoustic frequency of the thermal acoustic signal, respectively. For our breast model, the acoustic pressure rise is $p = 100$ Pa, and the

TABLE II
ACOUSTIC PARAMETERS FOR BIOLOGICAL TISSUES.
(* f IS THE ACOUSTIC FREQUENCY AND THE UNIT IS MEGAHERTZ)

Tissue	Breast	Skin	Muscle	Tumor
$\rho\ (kg/m^3)$	1020	1100	1041	1041
$c\ (m/s)$	1510	1537	1580	1580
$\alpha^*\ (dB/cm)$	$0.75f^{1.5}$	3.5	$0.57f$	$0.57f$
$\beta\ (1/^\circ C)$	3E-4	3E-4	3E-4	3E-4
$C_p\ (J/(^\circ C \cdot kg))$	3550	3500	3510	3510

maximal acoustic frequency is $f_{\max} = 500$ KHz. By substituting the parameters into (33), we obtain the shock distance in breast tissues to be

$$\begin{aligned}\chi_s &= \frac{\frac{B}{2A}}{2\left(\frac{B}{2A}+1\right)} \cdot \frac{\rho_0 c^2}{p} \cdot \frac{c}{f_{\max}} \\ &= \frac{5}{2(5+1)} \cdot \frac{1000 \cdot 1500^2}{100} \cdot \frac{1500}{500 \times 10^3} \\ &= 2.8 \times 10^4 \text{ m}. \end{aligned} \tag{34}$$

Because the size of our breast model is only 10 cm, which is much smaller than the shock distance, it is reasonable to ignore the nonlinear acoustic effect in the microwave-induced TAI system.

The two basic linear acoustic wave generation equations are [13]

$$\rho \frac{\partial}{\partial t}\mathbf{u}(\mathbf{r},t) = -\nabla p(\mathbf{r},t) \tag{35}$$

and

$$\nabla \cdot \mathbf{u}(\mathbf{r},t) = -\frac{1}{\rho c^2}\frac{\partial}{\partial t}p(\mathbf{r},t) + \alpha p(\mathbf{r},t) + \beta \frac{\partial}{\partial t}T(\mathbf{r},t) \tag{36}$$

where $\mathbf{u}(\mathbf{r},t)$ is the acoustic velocity vector, $p(\mathbf{r},t)$ is the acoustic pressure field, ρ is the mass density, α is the attenuation coefficient, β is the thermal expansion coefficient, and $T(\mathbf{r},t)$ is the temperature. The values for these acoustic properties for different breast tissues are listed in Table II [14], [46], [48]–[50]. The attenuation coefficient is calculated with $f = 0.15$ MHz. The values for the tumor are approximated using the values for muscle because we cannot find the values specific to the tumor.

Because the duration of the microwave pulse is much shorter than the thermal diffusion time, thermal diffusion can be neglected [13], and the thermal equation is

$$C_p \frac{\partial}{\partial t}T(\mathbf{r},t) = \text{SAR}(\mathbf{r},t) \tag{37}$$

where C_p is the specific heat. Substituting (37) into (36) gives

$$\nabla \cdot \mathbf{u}(\mathbf{r},t) = -\frac{1}{\rho c^2}\frac{\partial}{\partial t}p(\mathbf{r},t) + \alpha p(\mathbf{r},t) + \frac{\beta}{C_p}\text{SAR}(\mathbf{r},t). \tag{38}$$

FDTD is used again to compute the thermal acoustic wave based on (35) and (38). More details about FDTD for acoustic simulations can be found in [34], [35], and [51]–[57].

The breast model for the acoustic simulation is constructed similarly to the model for electromagnetic simulation. The velocities of the normal fatty breast tissue are also assumed random with a variation of $\pm 5\%$ around average values, as shown in Fig. 6(b). An acoustic sensor array with 35 elements deployed uniformly around the breast model is used to record the thermal acoustic signals. The distance between neighboring acoustic sensors is 4 mm. The grid cell size used by the acoustic FDTD is 0.1×0.1 mm and the computational region is terminated by PML absorbing boundary conditions [55]–[57]. Note that the size of the FDTD cell for acoustic simulation is much finer than that of the FDTD cell for electromagnetic simulation because the wavelength of an acoustic wave is much smaller than that of a microwave. The SAR distribution data is interpolated to achieve the designed grid resolution for the acoustic breast model.

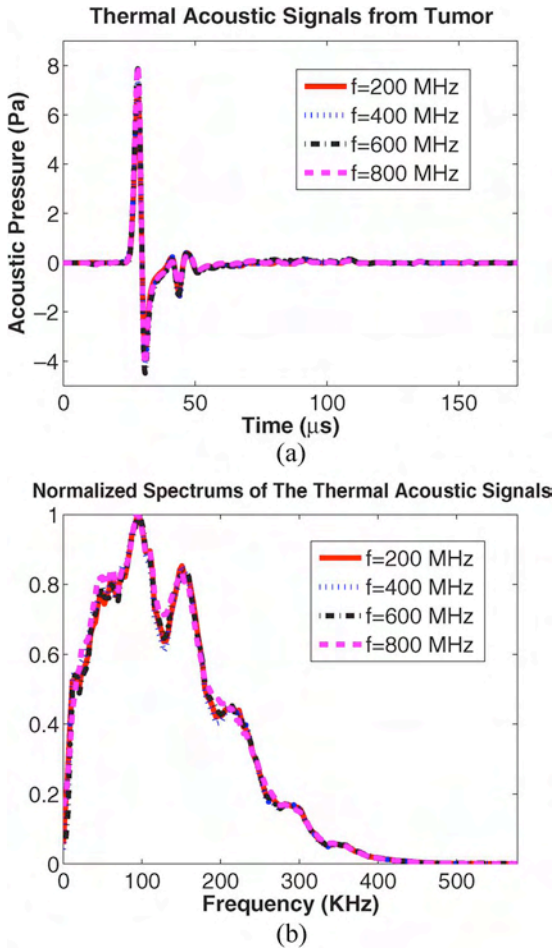

Fig. 8. Thermal acoustic signals at different stimulating frequencies $f = 200$, 400, 600, and 800 MHz. (a) Thermal acoustic responses from tumor only and (b) the normalized spectrums of the signals in (a).

V. NUMERICAL EXAMPLES

At the beginning of this section, the typical microwave-induced thermal acoustic responses from the tumor are plotted in Fig. 8(a) for stimulating frequencies of $f = 200$, 400, 600, and 800 MHz. The signals are simulated based on the aforementioned 2-D breast model. To obtain the signals, we perform the simulation twice at each stimulating frequency, with and

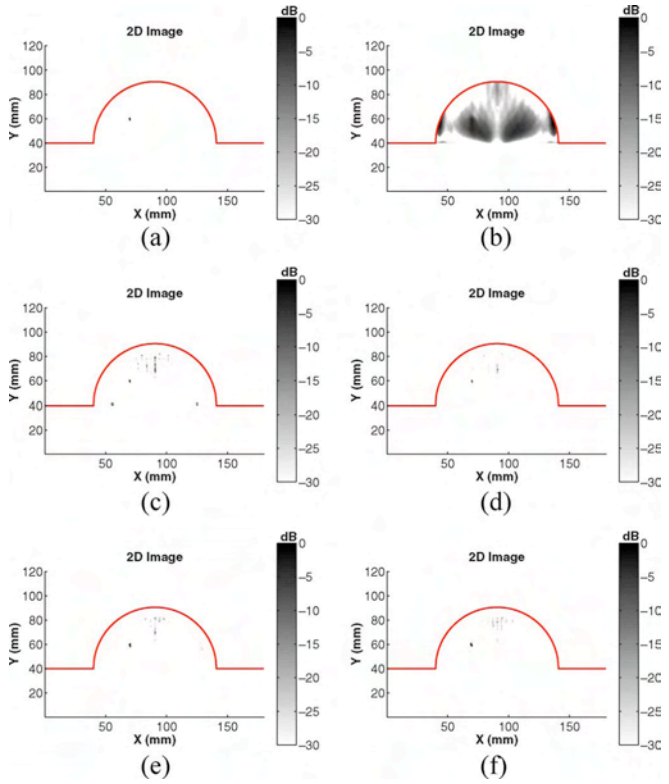

Fig. 9. Imaging results for the case of a single 1 mm-diameter tumor. (a) MART, (b) DAS, (c) SART at stimulating frequency $f = 200$ MHz, (d) SART at stimulating frequency $f = 400$ MHz, (e) SART at stimulating frequency $f = 600$ MHz, and (f) SART at stimulating frequency $f = 800$ MHz.

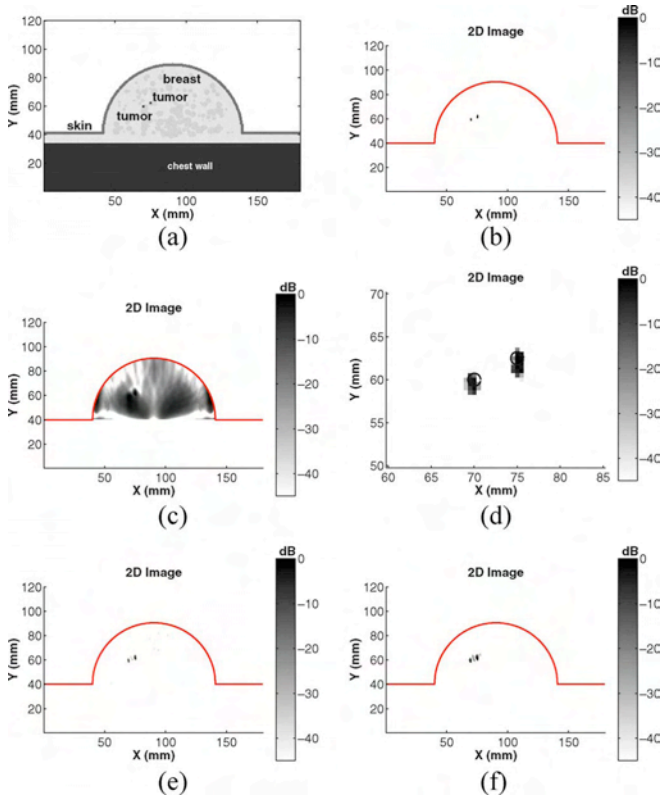

Fig. 10. Imaging results for the two 1.5-mm-diameter tumors case. (a) Breast model, (b) MART, (c) DAS, (d) zoom in of (b), (e) SART at stimulating frequency $f = 300$ MHz, and (f) SART at stimulating frequency $f = 700$ MHz.

without the tumor, and record the acoustic signals in an acoustic sensor. The difference of the two received signals is referred to as the thermal acoustic response only from the tumor at the stimulating frequency. It can be seen that the thermal acoustic responses from the tumor at different stimulating frequencies are similar to one another. The figure also shows that the thermal acoustic signals are wideband bipolar pulses, with a large positive peak and a large negative peak. Fig. 8(b) shows the normalized spectra of the acoustic signals corresponding to the excitations in Fig. 8(a). It is seen that the frequency range of the acoustic signals is about from 1 to 400 KHz. The dominant band (3-dB band) of the signals ranges from 10 to 180 KHz, and the corresponding acoustic wavelength ranges from 150 to 8 mm in the breast tissues.

Several numerical examples are used in this section to demonstrate the effectiveness of MART. The thermal acoustic signals are simulated based on the 2-D breast model with tumor only. For comparison purposes, the DAS method is applied to the same data set also. We also present the imaging results for the single-frequency microwave-induced TAI at different stimulating frequencies. The corresponding image reconstruction method is referred to as the single-frequency adaptive and robust technique (SART), which is similar with MART but without Stage II of MART. In SART, the RCB is used to estimate the thermal acoustic waveform at a certain stimulating frequency just like in Stage I of MART. Then the peak search method used in MART Stage III is applied to the estimated waveform to determine the image intensity.

In the first example, a 1-mm-diameter tumor is embedded in the breast model at the location ($x = 70$ mm, $y = 60$ mm). This is the challenging case of early breast cancer detection because of the small tumor size. Fig. 9(a) and (b) shows the imaging results for MART and DAS, respectively. The tumor is shown clearly in the MART image [Fig. 9(a)], and the size and location of the tumor is accurate. Because of the high sidelobe, poor resolution, and poor interference rejection capability of the DAS method, the tumor is essentially missed by DAS as shown in Fig. 9(b). Fig. 9(c)–(f) shows the imaging results for SART at the stimulating frequencies $f = 200$, 400, 600, and 800 MHz, respectively. The figures show that SART can determine the tumor correctly, but some clutter shows up in the SART images. Note that the clutter shows up at different locations with different stimulating frequencies. By comparing the images for MART and SART, it can be seen that the clutter are effectively suppressed by MART when multiple stimulating frequencies are used.

In the second numerical example, two small 1.5-mm-diameter tumors are set inside the breast model as shown in Fig. 10(a). Their locations are at ($x = 70$ mm, $y = 60$ mm) and ($x = 75$ mm, $y = 62.5$ mm). The distance between the two tumors is 4 mm. The imaging results using MART and DAS are shown in Fig. 10(b) and (c), respectively. The two tumors are seen clearly in the MART image. To show them clearly we zoom in onto the tumor locations in Fig. 10(d), where the two black circles mark the actual sizes and locations of the two tumors. It is shown that MART can be used to determine the locations and sizes of the two tumors accurately. The DAS

image contains much clutter. The two tumors cannot be separated clearly in the DAS image because of the poor resolution of DAS. Fig. 10(e) and (f) shows the imaging results of SART at stimulation frequencies $f = 300$ and 700 MHz, respectively. The tumors can be seen in both of the SART images, but clutter shows up between the two tumors in Fig. 10(e) and (f), and the sizes of the two tumors in Fig. 10(f) are larger than their true sizes.

VI. Conclusion

An investigation of using a multifrequency microwave-induced TAI system for early breast cancer detection has been reported in this paper. The frequency band for this system has been given based on the cutoff frequency of the human breast. A simplified semicircular dielectric waveguide mode was used to calculate the cutoff frequency in this paper. By studying the microwave energy absorption properties of breast tissue and tumor, we have shown that the multifrequency microwave-induced TAI can offer higher SNR, higher imaging contrast, and more effective clutter suppression capability than the traditional single-frequency microwave-induced TAI. A MART has been presented for image formation. This data-adaptive algorithm can achieve better resolution and better interference rejection capability than its data-independent counterparts, such as DAS. The feasibility of this multifrequency microwave-induced TAI system as well as the performance of the proposed image reconstruction algorithm for early breast cancer detection have been demonstrated by using 2-D numerical electromagnetic and acoustic breast models. The absorbed microwave energy and the thermal acoustic field in the breast models have been simulated using the FDTD method. Numerical examples have been used to demonstrate the excellent performance of this multifrequency technique. More advanced models are being developed to further investigate and validate the preferential imaging capability of the technique for early breast cancer detection.

References

[1] E. C. Fear, P. M. Meaney, and M. A. Stuchly, "Microwaves for breast cancer detection," *IEEE Potentials*, vol. 22, no. 1, pp. 12–18, Feb./Mar. 2003.

[2] P. M. Meaney, M. W. Fanning, D. Li, S. P. Poplack, and K. D. Paulsen, "A clinical prototype for active microwave imaging of the breast," *IEEE Trans. Microw. Theory Tech.*, vol. 48, no. 11, pp. 1841–1853, Nov. 2000.

[3] E. J. Bond, X. Li, S. C. Hagness, and B. D. Van Veen, "Microwave imaging via space-time beamforming for early detection of breast cancer," *IEEE Trans. Antennas Propagat.*, vol. 51, no. 8, pp. 1690–1705, Aug. 2003.

[4] B. Guo, Y. Wang, J. Li, P. Stoica, and R. Wu, "Microwave imaging via adaptive beamforming methods for breast cancer detection," *J. Electromagn. Waves Appl.*, vol. 20, no. 1, pp. 53–63, Jan. 2006.

[5] Y. Xie, B. Guo, L. Xu, J. Li, and P. Stoica, "Multi-static adaptive microwave imaging for early breast cancer detection," *IEEE Trans. Biomed. Eng.*, vol. 53, no. 8, pp. 1647–1657, Aug. 2006.

[6] D. Li, P. M. Meaney, and K. D. Paulsen, "Conformal microwave imaging for breast cancer detection," *IEEE Trans. Microw. Theory Tech.*, vol. 51, no. 4, pp. 1179–1186, Apr. 2003.

[7] Q. F. Fang, P. M. Meaney, S. D. Geimer, A. V. Streltsov, and K. D. Paulsen, "Microwave image reconstruction from 3-D fields coupled to 2-D parameter estimation," *IEEE Trans. Med. Imag.*, vol. 23, no. 4, pp. 475–484, Apr. 2004.

[8] Q. H. Liu, Z. Q. Zhang, T. T. Wang, J. A. Bryan, G. A. Ybarra, L. W. Nolte, and W. T. Joines, "Active microwave imaging I—2-D forward and inverse scattering methods," *IEEE Trans. Microw. Theory Tech.*, vol. 50, no. 1, pp. 123–133, Jan. 2002.

[9] Z. Q. Zhang, Q. H. Liu, C. Xiao, E. Ward, G. Ybarra, and W. T. Joines, "Microwave breast imaging: 3-D forward scattering simulation," *IEEE Trans. Biomed. Eng.*, vol. 50, no. 10, pp. 1180–1189, Oct. 2003.

[10] R. K. Mishra, A. Swarup, and J. M. Thomas, "Dielectric properties of normal and malignant human breast tissues at radiowave and microwave frequencies," *Ind. J. Biochem. Biophys.*, vol. 21, pp. 76–79, Feb. 1984.

[11] A. J. Surowiec, S. S. Stuchly, J. R. Barr, and A. Swarup, "Dielectric properties of breast carcinoma and the surrounding tissues," *IEEE Trans. Biomed. Eng.*, vol. 35, no. 4, pp. 257–263, Apr. 1988.

[12] W. T. Joines, Y. Zhang, C. X. Li, and R. L. Jirtel, "The measured electrical properties of normal and malignant human tissues from 50 to 900 MHz," *Med. Phys.*, vol. 21, no. 4, pp. 547–550, Apr. 1994.

[13] M. Xu and L. V. Wang, "Time-domain reconstruction for thermoacoustic tomography in a speherical geometry," *IEEE Trans. Med. Imag.*, vol. 21, no. 7, pp. 814–822, Jul. 2002.

[14] T. Szabo, *Diagnostic Ultrasound Imaging: Inside Out*. Burlington, MA: Elsevier, 2004.

[15] F. W. Kremkau, *Diagnostic Ultrasound: Principles and Instruments*. Philadelphia, PA: Saunders, 1993.

[16] E. Steen and B. Olstad, "Volume rendering of 3-D medical ultrasound data using direct feature mapping," *IEEE Trans. Med. Imag.*, vol. 13, no. 6, pp. 517–525, Jun. 1994.

[17] W. Joines, R. Jirtle, M. Rafal, and D. Schaeffer, "Microwave power absorption diffrences between normal and malignant tissue," *Int. J. Radiat. Oncol. Biol. Phys.*, vol. 6, no. 6, pp. 681–687, 1980.

[18] Y. Xu and L. H. Wang, "Effects of acoustic heterogeneity in breast thermoacoustic tomography," *IEEE Trans. Ultrason. Ferroelect. Freq. Control*, vol. 50, no. 9, pp. 1134–1146, Sep. 2003.

[19] M. Xu, Y. Xu, and L. V. Wang, "Time-domain reconstruction algorithms and numerical simulations for thermoacoustic tomography in various geometries," *IEEE Trans. Biomed. Eng.*, vol. 50, no. 9, pp. 1086–1099, Sep. 2003.

[20] Y. Xu, P. Kuchment, and L. H. Wang, "Limited-view thermoacoustic tomography and reconstruction by truncated conjugate gradient," *Med. Phys.*, vol. 31, pp. 724–733, Apr. 2004.

[21] R. A. Kruger, K. K. Kopecky, A. M. Aisen, D. R. Reinecke, G. A. Kruger, and W. L. Kiser, "Thermoacoustic CT with radio waves: A medical imaging paradigm," *Radiology*, vol. 211, pp. 275–278, Apr. 1999.

[22] R. A. Kruger, K. D. Miller, H. E. Reynolds, W. L. Kiser, D. R. Reinecke, and G. A. Kruger, "Breast cancer in vivo: Contrast enhancement with thermoacoustic CT at 434 MHz—Feasibility study," *Radiology*, vol. 216, pp. 279–283, Jul. 2000.

[23] R. A. Kruger, W. L. Kiser, K. D. Miller, H. E. Reynolds, D. R. Reinecke, and G. A. Kruger, "Thermoacoustic CT," in *Proc. IEEE MTT-S Int. Microwave Symp. Dig.*, Jun. 2000, vol. 2, pp. 11–16.

[24] Y. Xu, D. Feng, and L. H. Wang, "Exact frequency-domain reconstruction for thermoacoustic tomography I: Planar geometry," *IEEE Trans. Med. Imag.*, vol. 21, no. 7, pp. 823–828, Jul. 2002.

[25] Y. Xu, M. Xu, and L. H. Wang, "Exact frequency-domain reconstruction for thermoacoustic tomography II: Cylindrical geometry," *IEEE Trans. Med. Imag.*, vol. 21, no. 7, pp. 829–833, Jul. 2002.

[26] J. Li, P. Stoica, and Z. Wang, "On robust capon beamforming and diagonal loading," *IEEE Trans. Signal Process.*, vol. 51, no. 7, pp. 1702–1715, Jul. 2003.

[27] J. Li and P. Stoica, Eds., *Robust Adaptive Beamforming*. New York: Wiley, 2005.

[28] Y. Xie, B. Guo, J. Li, and P. Stoica, "Novel multistatic adaptive microwave imaging methods for early breast cancer detection," *EURASIP J. Appl. Signal Process.*, vol. 2006, pp. 1–12, 2006.

[29] Y. Xie, B. Guo, J. Li, G. Ku, and L. V. Wang, "Adaptive and robutst techniques (ART) for thermoacoustic tomography," presented at the Proc. 40th Asilomar Conf. Signals, Systems and Computers, Pacific Grove, CA, Nov. 2006.

[30] A. Taflove and S. C. Hagness, *Computational Electrodynamics: The Finite-Difference Time-Domain Method*, 2nd ed. Boston, MA: Artech House, 2000.

[31] D. M. Sullivan, *Electromagnetic Simulation Using the FDTD Method*. New York: IEEE, 2000.

[32] P. Bernardi, M. Cavagnaro, S. Pisa, and E. Piuzzi, "Specific absorption rate and temperature elevation in a subject exposed in the far-field of radio-frequency sources operating in the 10–900-MHz range," *IEEE Trans. Biomed. Eng.*, vol. 50, no. 3, pp. 295–304, Mar. 2003.

[33] P. Bernardi, M. Cavagnaro, S. Pisa, and E. Piuzzi, "SAR distribution and temperature increase in an anatomical model of the human eye exposed to the field radiated by the user antenna in a wireless LAN," *IEEE Trans. Microw. Theory Tech.*, vol. 46, no. 12, pp. 2074–2082, Dec. 1998.

[34] J. G. Maloney and K. E. Cummings, "Adaptation of FDTD techniques to acoustic modeling," in *Proc. 11th Annu. Rev. Progress in Applied Computational Electromagnetics*, Monterey, CA, 1995, vol. 2, pp. 724–731.
[35] X. Yuan, D. Borup, J. Wiskin, M. Berggren, and S. A. Johnson, "Simulation of acoustic wave propagation in dispersive media with relaxation losses by using FDTD method with PML absorbing boundary condition," *IEEE Trans. Ultrason., Ferroelect., Freq. Control*, vol. 46, no. 1, pp. 14–23, Jan. 1999.
[36] C. A. Balanis, *Advanced Engineering Electromagnetics*. New York: Wiley, 1989.
[37] S. Yang, H. Kim, and H. J. Lee, "Circular-harmonic vector analysis of dielectric waveguide with a cross-cut-circle cross section," *Appl. Opt.*, vol. 34, pp. 7705–7713, Nov. 1995.
[38] S. Gabriel, R. W. Lau, and C. Gabriel, "The dielectric properties of biological tissues: III. Parametric models for the dielectric spectrum of tissues," *Phys. Med. Biol.*, vol. 41, pp. 2271–2293, Nov. 1996.
[39] C. Gabriel and S. Gabriel, "Compilation of the dielectric properties of body tissues at rf and microwave frequencies," [Online]. Available: http://www.brooks.af.mil/AFRL/HED/hedr/reports/dielectric/home.html
[40] "Dielectric properties of body tissues," [Online]. Available: http://niremf.ifac.cnr.it/tissprop/
[41] X. Li and S. C. Hagness, "A confocal microwave imaging algorithm for breast cancer detection," *IEEE Microw. Wireless Compon. Lett.*, vol. 11, no. 3, pp. 130–132, Mar. 2001.
[42] P. Stoica and R. L. Moses, *Spectral Analysis of Signals*. Upper Saddle River, NJ: Prentice-Hall, 2005.
[43] C. G. A. Hoelen and F. F. M. de Mul, "Image reconstruction for photoacoustic scanning of tissue structures," *Appl. Opt.*, vol. 39, pp. 5872–5883, Nov. 2000.
[44] S. D. Gedney, "An anisotropic perfectly matched layer-absorbing medium for the truncation of FDTD lattices," *IEEE Trans. Antennas Propagat.*, vol. 44, no. 12, pp. 1630–1639, Dec. 1996.
[45] Z. S. Sacks, D. M. Kingsland, R. Lee, and J. F. Lee, "A perfectly matched anisotropic absorber for use as an absorbing boundary condition," *IEEE Trans. Antennas Propagat.*, vol. 43, no. 12, pp. 1460–1463, Dec. 1995.
[46] M. Xu and L. H. Wang, "Pulsed-microwave-induced thermoacoustic tomography: Filtered backprojection in a circular measurement configuration," *Med. Phys.*, vol. 29, no. 8, pp. 1661–1669, Aug. 2002.
[47] M. F. Hamilton and D. T. Blackstock, *Nonlinear Acoustics*. San Diego, CA: Acadmic, 1997.
[48] F. A. Duck, *Physical Properties of Tissue*. London, U.K.: Academic, 1990.
[49] M. L. Palmeri and K. R. Nightingale, "On the thermal effects associated with radiation force imaging of soft tissue," *IEEE Trans. Ultrason., Ferroelect., Freq. Control*, vol. 51, no. 5, pp. 551–565, May 2004.
[50] M. Converse, E. J. Bond, S. C. Hagness, and B. D. Van Veen, "Ultra-wide-band microwave space-time beamforming for hyperthermia treatment of breast cancer: A computational feasibility study," *IEEE Trans. Microw. Theory Tech.*, vol. 52, no. 8, pp. 1876–1889, Aug. 2004.
[51] C. K. W. Tam and J. C. Webb, "Dispersion-relation-preserving finite-difference schemes for computational acoustics," *J. Comput. Phys.*, vol. 107, no. 8, pp. 262–281, Aug. 1993.
[52] S. V. Tsynkov, "Numerical solution of problems on unbounded domains. A review," *Appl. Numer. Math.*, vol. 27, pp. 465–532, Aug. 1998.
[53] T. Colonius, S. K. Lele, and P. Moin, "Boundary-conditions for direct computation of aerodynamic sound generation," *AIAA J.*, vol. 31, pp. 1574–1582, Sep. 1993.
[54] C. W. Rowley and T. Colonius, "Discretely nonreflecting boundary conditions for linear hyperbolic systems," *J. Comput. Phys.*, vol. 157, pp. 500–538, Jan. 2000.
[55] Q. H. Liu and J. Tao, "The perfectly matched layer for acoustic waves in absorptive media," *J. Acoust. Soc. Amer.*, vol. 102, pp. 2072–2082, October 1997.
[56] X. Yuan, D. Borup, J. W. Wiskin, M. Berggren, R. Eidens, and S. A. Johnson, "Formulation and validation of Berenger's PML absorbing boundary for the FDTD simulation of acoustic scattering," *IEEE Trans. Ultrason., Ferroelect., Freq. Control*, vol. 44, no. 7, pp. 816–822, Jul. 1997.
[57] T. K. Katsibas and C. S. Antonopoulos, "A general form of perfectly matched layers for three-dimensional problems of acoustic scattering in lossless and lossy fluid media," *IEEE Trans. Ultrason., Ferroelect., Freq. Control*, vol. 51, no. 8, pp. 964–972, Aug. 2004.

Bin Guo (S'06–M'07) received the B.E. and M.Sc. degrees in electrical engineering from Xian Jiaotong University, Xian, China, in 1997 and 2000, respectively. He is currently pursuing the Ph.D. degree in electrical engineering in the Department of Electrical and Computer Engineering, University of Florida, Gainesville.

From April 2002 to July 2003, he was an Associate Research Scientist with the Temasek Laboratories, National University of Singapore, Singapore. Since August 2003, he has been a Research Assistant with the Department of Electrical and Computer Engineering, University of Florida. His current research interests include biomedical applications of signal processing, microwave imaging, and computational electromagnetics.

Jian Li (S'88–M'90–SM'97–F'05) received the M.Sc. and Ph.D. degrees in electrical engineering from The Ohio State University, Columbus, in 1987 and 1991, respectively.

From July 1991 to June 1993, she was an Assistant Professor with the Department of Electrical Engineering, University of Kentucky, Lexington. Since August 1993, she has been with the Department of Electrical and Computer Engineering, University of Florida, Gainesville, where she is currently a Professor. Her current research interests include spectral estimation, statistical and array signal processing, and their applications.

Dr. Li is a fellow of Institution of Electrical Engineers (IEE). She received the 1994 National Science Foundation Young Investigator Award and the 1996 Office of Naval Research Young Investigator Award. She has been a member of the Editorial Board of Signal Processing, a publication of the European Association for Signal Processing (EURASIP) since 2005. She is presently a member of two of the IEEE Signal Processing Society technical committees: the Signal Processing Theory and Methods (SPTM) Technical Committee and the Sensor Array and Multichannel (SAM) Technical Committee.

Henry Zmuda (M'75) received the B.E. degree from the Stevens Institute of Technology, Hoboken, NJ, in 1979, and the M.S. and Ph.D. degrees from Cornell University, Ithaca, NY, in 1982 and 1984, respectively, all in electrical engineering.

From 1984 to 1995, he was a member of the faculty at Stevens Institute of Technology. In 1995, he joined the Electrical Engineering Faculty, University of Florida. His research interests are primarily in the area of microwave photonics and applied electromagnetics.

Mark Sheplak received the B.S. degree in 1989, the M.S. degree in 1992, and the Ph.D. degree in 1995 in mechanical engineering from Syracuse University, Syracuse, NY.

He is an Associate Professor in the Department of Aerospace and Mechanical Engineering and an Affiliate Associate Professor of electrical and computer engineering at the University of Florida (UF). Prior to joining UF in 1998, he was a Postdoctoral Associate at the Massachusetts Institute of Technology's Microsystems Technology Laboratories, Cambridge, from 1995 to 1998. During his Ph.D. studies, he was a GSRP Fellow at the NASA-Langley Research Center, Hampton, VA, from 1992 to 1995. His current research focuses on the design, fabrication, and characterization of high-performance, instrumentation-grade, MEMS-based sensors and actuators that enable the measurement, modeling, and control of various physical properties.

Adaptive and Robust Techniques (ART) for Thermoacoustic Tomography in Breast Cancer Detection

Yao Xie† Bin Guo† Jian Li†
†Dept. of Electrical and Computer Engineering
University of Florida
P. O. Box 116130, Gainesville, FL 32611, USA.

Geng Ku‡ Lihong Wang‡
‡Dept. of Biomedical Engineering
Texas A&M University
3120 TAMU, College Station, TX 77843-3120, USA.

[1] ***Abstract*— We present Adaptive and Robust Techniques (ART) for thermoacoustic tomography with application in breast cancer detection. TAT combines high contrast and high resolution. The current image reconstruction methods used for TAT, such as the widely used Delay-and-Sum (DAS) approach, are data-independent and suffer from low resolution, high sidelobe levels, and poor interference rejection capabilities. The data-adaptive ART have much better performance than their data-independent counterparts. By allowing certain uncertainties, ART can mitigate the amplitude and phase distortion problems encountered in TAT. The excellent performance of ART is demonstrated using both simulated and experimentally measured data.**

I. Introduction

Thermoacoustic tomography (TAT) [1] is a new technology with great promise in a wide span of biomedical applications. In TAT, an image of the tissue radiation absorption properties is reconstructed from the recorded thermoacoustic signals. Such an image reveals the physiological and pathological status of the tissue, which has been used in many applications including breast cancer detection. Microwave-induced TAT combines the high contrast of biological tissue in electromagnetic frequency band and the millimeter range spatial resolution due to the acoustic signals used [2].

Developing accurate and robust image reconstruction methods is one of the key challenges encountered in TAT. Time-domain approximate reconstruction algorithms such as the DAS [3] (weighted or unweighted) type of data-independent approaches are widely used. They need little prior information on the tissue for image reconstruction and can be fast and simple to implement to process the wideband acoustic signals. Although not based on the exact solution, they provide similar image qualities to those of the exact reconstruction algorithms. However, these data-independent methods suffer from poor resolution and high sidelobe level problems. Data-adaptive approaches, such as the recently introduced Robust Capon Beamforming (RCB) method [4], can have much better resolution and much better interference rejection capability than their data-independent counterparts.

[1]This research was supported in part by the National Institutes of Health (NIH) Grant No. 1R41CA107903-1.

A common assumption of the existing methods is that the surrounding tissue is acoustically homogeneous. This approximation is inadequate in many medical imaging applications. According to previous studies, the sound speed in human female breast varies widely from 1430 m/s to 1570 m/s around the commonly assumed speed of 1510 m/s [5]. The heterogeneous acoustic properties of biological tissues cause amplitude and phase distortions in the recorded acoustic signals, which can result in significant degradations in image quality [6]. Although various methods have been proposed for the amplitude and phase distortions in Ultra-sound Tomography (UT), the problem in TAT is somewhat different: in TAT, for the breast tissue with a relatively weak heterogeneity, phase distortion dominates amplitude distortion [6].

We propose Adaptive and Robust Techniques (ART) based on RCB for TAT. ART can be used to mitigate the amplitude and phase distortion problems in TAT by allowing certain uncertainties. We will demonstrate the excellent performance of ART by using both data simulated on a 2-D breast model and data experimentally measured from mastectomy specimens.

II. Problem Formulation

Consider a TAT imaging system as shown in Figure 1(a). A stimulating microwave pulse is absorbed by the biological tissue under testing, which causes a sudden heat change. Due to the thermoacoustic effect, an acoustic pulse is generated which can be recorded by an ultrasonic transducer array (a real aperture array or a synthetic aperture array). The number of transducers in the array (or the number of transducer data acquisition locations in the synthetic aperture array) is M. Each transducer is assumed to be omnidirectional.

The data model for the sampled and digitized acoustic signal recorded by the mth transducer is given by:

$$x_m(n) = s_m(n) + \tilde{e}_m(n), \quad m = 1, \cdots, M. \tag{1}$$

where n is the discrete time index, starting from t_0 after excitation pulse. The scalar $s_m(n)$ denotes the signal component, which corresponds to the acoustic pulse generated at a focal point, and $\tilde{e}_m(n)$ is the residual term, which includes unmodelled noise and interference.

The goal of ART is to reconstruct an image of thermoacoustic response intensity $I(\mathbf{r})$, which is directly related to the absorption property of the tissue, from the recorded data set $\{x_m(n)\}$. Herein the vector $\mathbf{r}$ denotes the focal point location coordinate. To form an image, we scan the focal point at location $\mathbf{r}$ to cover the entire cross-section of the tissue.

The discrete arrival time of the pulse (for the mth transducer) can be determined approximately as:

$$t_m(\mathbf{r}) = \left\lfloor -\frac{t_0}{\Delta t} + \frac{\|\mathbf{r} - \mathbf{r}_m\|}{\Delta t v_0} \right\rfloor. \tag{2}$$

We will omit the dependence of the arrival time $t_m(\mathbf{r})$ on $\mathbf{r}$ hereafter for notational simplicity. Here Δt is the sampling interval, and the 3-D vector $\mathbf{r}_m$ denotes the location of the mth transducer. The sound speed v_0 is chosen to be the average sound speed of the biological tissue under interrogation. The notation $\|\mathbf{x}\|$ denotes the Euclidean norm of $\mathbf{x}$, and $\lfloor y \rfloor$ stands for rounding to the greatest integer less than y.

The signal components $\{s_m(n)\}_{m=1}^M$ are approximately scaled and shifted versions of a nominal waveform $s(t)$ at the source:

$$s_m(n) \approx \frac{\exp\left(-\alpha\|\mathbf{r} - \mathbf{r}_m\|\right)}{\|\mathbf{r} - \mathbf{r}_m\|} \cdot s(n - t_m), \tag{3}$$

where α is the attenuation coefficient in Nepers/m. We preprocess the data to time delay all the signals from the focal point $\mathbf{r}$ and compensate for the loss in amplitude due to propagation decay. Let $y_m(n)$ denote the signal after preprocessing to backpropagate the detected signal to the source:

$$y_m(n) = \exp\left(\alpha\|\mathbf{r} - \mathbf{r}_m\|\right) \cdot \|\mathbf{r} - \mathbf{r}_m\| x_m(n + t_m); \tag{4}$$

then the received vector data model can be written as:

$$\mathbf{y}(n) = \mathbf{a}_0 s(n) + \mathbf{e}(n), \quad n = -N, \cdots, N, \tag{5}$$

where $\mathbf{a}_0$ is the corresponding steering vector, which is approximately equal to $\bar{\mathbf{a}} = [1, \cdots, 1]^T$, $\mathbf{y}(n) = [y_1(n), \cdots, y_M(n)]^T$, $\mathbf{e}(n)$ represents the noise and interference term after preprocessing, and $(\cdot)^T$ denotes the transpose. The time interval of interests for the signal $\mathbf{y}(t)$ is from $-N$ to N, which is large enough to covers the expected signal duration in the region of interest.

In reality, both the amplitude and the phase (or pulse arrival time) of the acoustic pulse will be distorted. Amplitude distortion is mainly caused by multi-path in the heterogeneous medium. Phase distortion is due to the nonuniform sound speed, an inaccurate estimate of t_0, and the transducer calibration error. These distortions will blur the image, raise the image background noise level, and lower the values of the object of interest [6].

In ART, we mitigate the effects of these distortions by allowing $\mathbf{a}_0$ to belong to an uncertainty set centered at $\bar{\mathbf{a}}$ and by considering the signal arriving within the interval from $-N$ to N. Our ART algorithm consists of three steps: Step I, Robust Capon Beamforming (RCB) [4] for robust waveform estimation; Step II, peak-searching for phase aberration mitigation; Step III, intensity calculation for forming the final images.

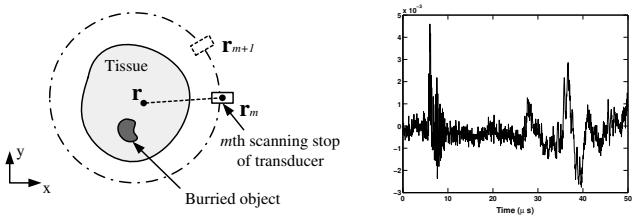

(a) (b)

Fig. 1. (a): A schematic of a 2-D synthetic aperture based TAT scanning system; (b): a typical acoustic pulse recorded by a transducer (for data measured from breast specimen II).

III. Step I of ART: Waveform Estimation

The first step of ART is to estimate the waveform of the acoustic pulse generated by the focal point at location $\mathbf{r}$, based on the data model in (5). It will appear that we have neglected the presence of phase distortion by using this data model in the first step. However, by allowing $\mathbf{a}_0$ to be uncertain, we can tolerate some phase distortions as well. This approximation causes little performance degradation to our robust algorithm.

Covariance fitting based RCB [4] is used to first estimate the steering vector $\mathbf{a}_0$, and use the estimated $\mathbf{a}_0$ to obtain an optimal beamformer weight vector for pulse waveform estimation. By assuming that the true steering vector lies in the vicinity of the nominal steering vector $\bar{\mathbf{a}}$, we consider the following optimization problem [4]:

$$\max_{\sigma^2, \mathbf{a}_0} \sigma^2 \quad \text{subject to} \quad \hat{\mathbf{R}} - \sigma^2 \mathbf{a}_0 \mathbf{a}_0^T \geq 0, \quad \|\mathbf{a}_0 - \bar{\mathbf{a}}\|^2 \leq \varepsilon, \tag{6}$$

where σ^2 is the power of the signal of interest, and

$$\hat{\mathbf{R}} = \frac{1}{2N+1} \sum_{n=-N}^{N} \mathbf{y}(n)\mathbf{y}^T(n) \tag{7}$$

is the sample covariance matrix. The second constraint in (6) is a spherical uncertainty set; an elliptical uncertainty set can be used instead if a tighter constraint is desirable [4].

The parameter ε in (6) determines the size of the uncertainty set and is a user parameter. To avoid the trivial solution of $\mathbf{a}_0 = 0$, we require that

$$\varepsilon < \|\bar{\mathbf{a}}\|^2. \tag{8}$$

To attain high resolution and to effectively suppress interference, ε should be made as small as possible. On the other hand, the smaller the sample size N or the larger the distortions, the larger should ε be chosen [4]. Since the performance of RCB does not depend very critically on the choice of ε, in our examples we choose certain reasonable initial values for ε, and then make some adjustments empirically based on image quality.

By using the Lagrange multiplier method, the solution to (6) is given by [4]:

$$\hat{\mathbf{a}}_0 = \bar{\mathbf{a}} - \left[\mathbf{I} + \mu\hat{\mathbf{R}}\right]^{-1} \bar{\mathbf{a}}, \tag{9}$$

where $\mathbf{I}$ is the identity matrix, $\mu \geq 0$ is the corresponding Lagrange multiplier that can be solved from the following equation:

$$\left\| (\mathbf{I} + \mu \hat{\mathbf{R}})^{-1} \bar{\mathbf{a}} \right\|^2 = \varepsilon. \tag{10}$$

Consider the eigendecomposition on the sample covariance matrix $\hat{\mathbf{R}}$:

$$\hat{\mathbf{R}} = \mathbf{U} \mathbf{\Gamma} \mathbf{U}^T, \tag{11}$$

where the columns of $\mathbf{U}$ are the eigenvectors of $\hat{\mathbf{R}}$ and the diagonal matrix $\mathbf{\Gamma}$ consists of the corresponding eigenvalues $\gamma_1 \geq \gamma_2 \geq \cdots \geq \gamma_M$. Let $\mathbf{b} = \mathbf{U}^T \bar{\mathbf{a}}$, where b_m denotes its mth element. Then (10) can be rewritten as

$$\mathcal{L}(\mu) = \sum_{m=1}^{M} \frac{|b_m|^2}{(1 + \mu \gamma_m)^2} = \varepsilon. \tag{12}$$

Note that $\mathcal{L}(\mu)$ is a monotonically decreasing function of μ, with $\mathcal{L}(0) > \varepsilon$ by (8) and $\lim_{\mu \to \infty} \mathcal{L}(\mu) = 0 < \varepsilon$, which means that μ can be solved efficiently, say, by using the Newton's method (see [4] for more details). After obtaining the value of μ, the estimate $\hat{\mathbf{a}}_0$ of the actual steering vector $\mathbf{a}_0$ is determined by (9).

Observe that there is a "scaling ambiguity" in (6) by treating both the signal power σ^2 and the steering vector $\mathbf{a}_0$ as unknowns (see [4]). To eliminate this ambiguity, we scale the solution $\hat{\mathbf{a}}_0$ to make its norm satisfy the following condition:

$$\|\hat{\mathbf{a}}_0\|^2 = M. \tag{13}$$

To obtain an estimate for the signal waveform $s(n)$, we apply a weight vector to the preprocessed signals $\{\mathbf{y}(n)\}_{n=-N}^{N}$. The weight vector is determined by using the estimated steering vector $\hat{\mathbf{a}}_0$ in the weight vector expression of the standard Capon beamformer (see, e.g., [4]):

$$\hat{\mathbf{w}}_{\text{RCB}} = \frac{\|\hat{\mathbf{a}}_0\|}{M^{1/2}} \cdot \frac{\left[\hat{\mathbf{R}} + \frac{1}{\mu}\mathbf{I}\right]^{-1} \bar{\mathbf{a}}_0}{\bar{\mathbf{a}}_0^T \left[\hat{\mathbf{R}} + \frac{1}{\mu}\mathbf{I}\right]^{-1} \hat{\mathbf{R}} \left[\hat{\mathbf{R}} + \frac{1}{\mu}\mathbf{I}\right]^{-1} \bar{\mathbf{a}}_0}. \tag{14}$$

Note that (14) has a diagonal loading form, which allows the sample covariance matrix to be rank-deficient. The beamformer output can be written as:

$$\hat{s}_{\text{RCB}}(n) = \hat{\mathbf{w}}_{\text{RCB}}^T \mathbf{y}(n), \quad n = -N, \cdots, N, \tag{15}$$

which is the waveform estimate for the acoustic pulse generated at the focal point at location $\mathbf{r}$.

RCB can provide a much better waveform estimate than the conventional DAS but at a higher computational cost. For a single focal point, RCB requires $O(M^3)$ flops, which mainly comes from the eigen-decomposition of the sample covariance matrix $\hat{\mathbf{R}}$ [4]; DAS needs only $O(M)$ flops. DAS can be used as a fast image reconstruction method to provide initial imaging results.

The weight vector used by DAS for waveform estimation is

$$\hat{\mathbf{w}}_{\text{DAS}} = \bar{\mathbf{a}}, \tag{16}$$

and the estimated waveform is given by

$$\hat{s}_{\text{DAS}}(n) = \hat{\mathbf{w}}_{\text{DAS}}^T \mathbf{y}(n) = \sum_{m=1}^{M} y_m(n), \quad n = -N, \cdots, N. \tag{17}$$

IV. Step II of ART: Peak Searching

Based on the estimated waveform obtained in Step I for the focal point at location $\mathbf{r}$, in Step II of ART, we will search for the two peaks of the bipolar acoustic pulse generated by the focal point. In a homogeneous background we can accurately calculate the arrival time of the acoustic pulse generated by the focal point at location $\mathbf{r}$ by using (2); this is not true in heterogeneous biological tissues due to the nonuniform sound speed. We can assume that the original peak remains a peak in the waveform estimated from Step I of ART, since the amplitude distortion is not severe in TAT [6].

The bipolar acoustic pulse has one peak positive and another negative. We determine the positive and negative peak values as follows:

$$P^+ = \max \left\{ \max_{n \in [-\Delta, \Delta]} \hat{s}(n), 0 \right\}, \tag{18}$$

$$P^- = \min \left\{ \min_{n \in [-\Delta, \Delta]} \hat{s}(n), 0 \right\}, \tag{19}$$

where the searching range $[-\Delta, \Delta] \in [-N, N]$ is around the calculated arrival time given by (2). Here Δ is a user parameter. Since the peak searching is independent of the particular waveform estimation methods, we use $\hat{s}(n)$ to denote the waveform estimated by either DAS or ART.

The search range is determined by the difference between the true arrival time $\bar{t}_m$ and the calculated arrival time t_m based on (2). An expression the arrival time difference has been given in [6] in the following form:

$$\delta_m(\mathbf{r}') = \bar{t}_m - t_m \propto \frac{[v(\mathbf{r}') - v_0]}{v_0}, \tag{20}$$

where $\mathbf{r}'$ is a point within the line connecting the focal point at location $\mathbf{r}$ and the mth transducer at location $\mathbf{r}_m$, and $v(\mathbf{r}')$ is the local sound speed. In (20), the higher order terms of $[v(\mathbf{r}') - v_0]/v_0$ have been ignored. It is reasonable to assume that $v(\mathbf{r}')$ is Gaussian distributed with mean v_0 and variance σ_v^2. Consequently the arrival time difference is also Gaussian distributed with zero-mean and variance $\sigma_\delta^2 \propto \sigma_v^2 / v_0^2$. If we choose $\Delta = \sigma_\delta$, and the duration of the acoustic pulse is τ, we can find the two peaks of the pulse within the interval $(-\sigma_\delta, \sigma_\delta + \tau)$ on the recorded signals with a high probability of 0.6826. This analysis is consistent with the experimental measurements in [7]. From our examples, we found that a symmetric range $[-\Delta, \Delta]$ around the estimated arrival time performs similarly to the asymmetric range $[-\Delta, \Delta + \tau]$, and we use the former since it is easy to handle in practice. Also, we can use similar techniques as those in [7] to estimate σ_δ to find a good searching range for Step II of ART, and to estimate τ for the energy type methods in our examples.

There is a tradeoff in choosing the searching range. The larger the searching range, the higher the probability we can

find the peaks of the acoustic pulse within the range. However, if the range is chosen too large, the interferences may cause false peaks, and as a consequence, we are more likely to find a false peak. In our examples we choose the best searching range empirically based on the estimates of $\hat{\sigma}_\delta$.

V. Step III of ART: Intensity Calculation

Based on the estimation of the waveform generated by the focal point at location $\mathbf{r}$, the response intensity for need to be calculated. There are two major types of response intensity measurement approaches: amplitude based and energy based. They extract different information from the estimated waveform, which may be useful to physicians in different ways.

Conventional DAS uses the amplitude based measure for TAT imaging [3], with the corresponding response intensity given by $\hat{s}(0)$, or equivalently:

$$I_{\text{C}} = \hat{s}(0) = \sum_{m=1}^{M} y_m(0). \tag{21}$$

The energy based measure, such as the one used in the mono-static and multi-static microwave imaging for breast cancer detection [8], calculate the intensity by:

$$I_{\text{E}} = \sum_{n=0}^{\tau} \hat{s}^2(n) = \sum_{n=0}^{\tau} \left[\sum_{m=1}^{M} y_m(n) \right]^2, \tag{22}$$

We can consider using the peak value as the response intensity measure due to the bipolar nature of the response at the focal point:

$$I_{\text{P}} = \begin{cases} P^+ & \text{if } |P^+| \geq |P^-|; \\ P^- & \text{otherwise,} \end{cases} \tag{23}$$

Herein we keep the sign of the maximum amplitude since the sign of the peak may also contain some information about the focal point.

Peak-searching maximizes the output signal-to-noise ratio. An intuitive explanation is that, given the fact that the acoustic pulse is bipolar [3], if we assume that the residual term $\mathbf{e}(t)$ is stationary, or its power is uniform over time, then the signal-to-noise ratio is maximized at the (positive or negative) peak of the acoustic pulse. As a comparison, the conventional DAS (21) fixes the samples to be summed up at the calculated arrival time. Due to phase distortions, the waveform at the calculated time may be far from the peak value.

We can also employ peak-to-peak difference as the response intensity for the focal point at location $\mathbf{r}$:

$$I_{\text{PP}} = P^+ - P^- \geq 0. \tag{24}$$

Peak-to-peak difference has higher imaging contrast than peak value measure: the peak-to-peak difference of the bipolar pulse is approximately twice the absolute peak value, which means that the output signal power of the former is four times of the latter; yet the noise power of the former is only twice of the latter. Therefore the output Signal-to-Noise Ratio (SNR) is doubled by using the peak-to-peak difference rather than the peak value. Both peak-value and peak-to-peak difference measures belong to the amplitude based measures.

VI. Numerical and Experimental Examples

A. Numerical Examples

We simulate a 2-D cylindrical breast model using the Finite-Difference Time-Domain (FDTD) method. The 2-D breast model includes 2 mm thick skin, chest wall, as well as randomly distributed fatty breast tissues and glandular tissues. The cross-section of the breast model is a half circle with a 10 cm diameter. A 2 mm-diameter tumor is located at 2.2 cm below the skin (at $x = 7.0$ cm, $y = 6.0$ cm).

The dielectric properties of the breast tissues are assumed to be Gaussian random variables with variations of $\pm 10\%$ around their nominal values. The nominal values are chosen to be typical of those reported in the literature, which is given in Table 1 of [8]. The dispersive properties of the tissues are also considered in the model. Fat breast tissues and glandular tissues are randomly distributed in the breast model. The differential equations in [9] are used to characterize the thermoacoustic effect in our FDTD simulations.

We model the sound speed within the breast as a Gaussian random variable with variation $\pm 5\%$ around the assumed average sound speed of 1500 m/s. The probing microwave pulse used here is a modulated rectangular pulse with a modulating frequency of 800 MHz. The duration of the pulse is 1 μs. Before applying the aforementioned preprocessing steps and ART, we remove the strong skin response using techniques similar to those in [8]. In the following all the images are displayed on a linear scale, and we will name the imaging methods by their waveform estimation method followed by the intensity calculation approach, such as "DAS-C."

Figure 2 shows the images for the simulated breast model ART and DAS. The tumor response is weak for such a small tumor. In these images we use $\varepsilon = 0.1M$ and the searching range [-14, 14]. Figure 2(a) corresponds to DAS-C, where the tumor is buried by interference and noise. In Figure 2(b), for RCB-E, most of the clutters are cleared up but a strong clutter shows up near the chest wall. Images produced by ART-P in Figure 2(d) and by ART-PP in Figure 2(f) have lower sidelobe levels and higher resolutions than their DAS based counterparts. ART-PP has a higher contrast than the former, due to the peak-to-peak difference used as the intensity measure.

B. Experimental Results

We have also tested ART and DAS on some TAT experimental data obtained from a mastectomy specimen [2] by the Optical Imaging Laboratory at the Texas A&M University. In the experiment, the breast specimen was formed to a cylindrical shape inside a plastic bowl. The bowl was immersed in ultrasound coupling medium in a container. The acoustic signals were recorded at 240 equally spaced scanning stops on a circular track of radius 12.9 cm. The thickness of this specimen was about 4 cm in a round plastic bowl of 17 cm in diameter. This lesion was diagnosed as an invasive metaplastic carcinoma with chondroid and squamous metaplasia. The size of the tumor was measured to be 35 mm in diameter by TAT, and 36 mm in diameter by radiography (see [2] for details).

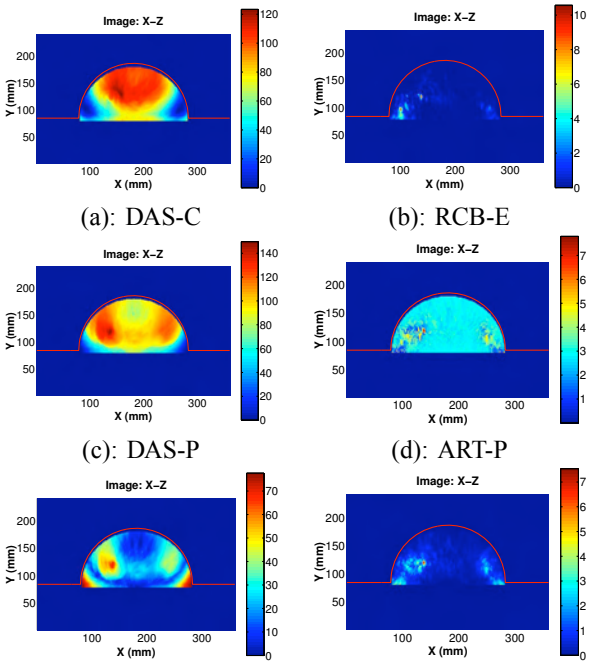

Fig. 2. Reconstructed images based on the 2-D simulated breast model with one 2 mm-diameter tumor.

Figure 3 shows the reconstructed images for the breast specimen. In the following images, the searching range was set to [-3, 3], and $\varepsilon = 0.5M$ for all the RCB used herein. In Figure 3(a), for DAS-C, the dark region shows an blurred object corresponding to the breast tumor. In 3(b), for RCB-E, the light region shows a vague boundary of the tumor. In Figures 3(c), for DAS-P, and 3(d), for ART-P, a dark region with a clear cut has a good correspondence with the location and shape of the tumor in the radiograph 3(g). In Figures 3(e), for DAS-PP, and 3(f), for ART-PP, not only a clear image of the tumor is obtained, but also the detailed boundary is revealed. For comparison, the images from X-ray mammography and the exact inverse solution of TAT (see [2] for more details) are shown in Figures 3(g) and 3(h), respectively.

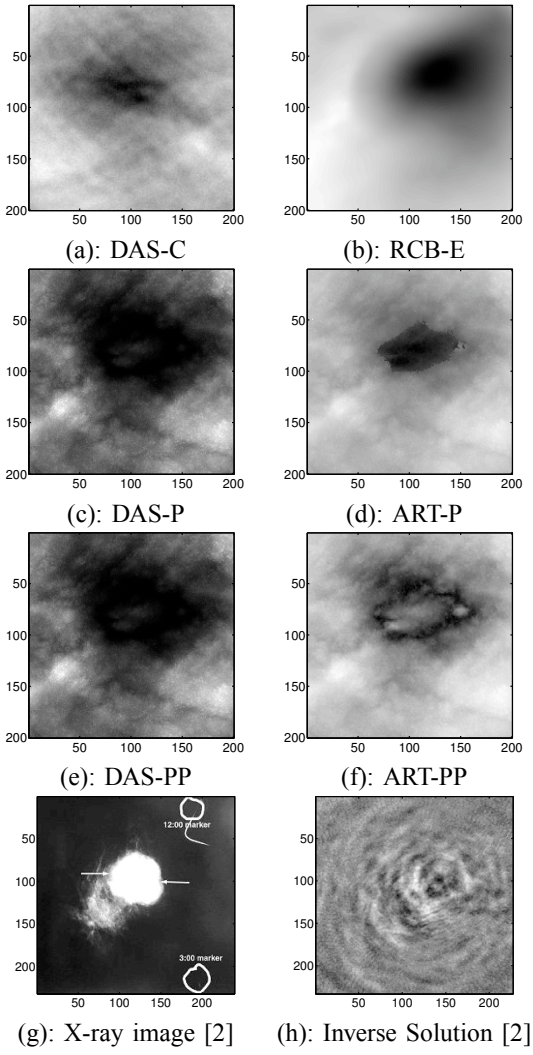

Fig. 3. Reconstructed images for the breast specimen.

VII. Conclusions

Adaptive and Robust Techniques (ART) have been proposed for thermoacoustic tomography. ART is robust to the amplitude and phase distortions in the recorded signals caused by the acoustic heterogeneity of biological tissues. Examples based on a numerically simulated 2-D breast model and experimentally measured data from human mastectomy specimens demonstrate the excellent performance of ART: high resolution, low-side lobe level, much better interference suppression capability. ART could detect tumors as small as 2-mm in diameter.

References

[1] R. A. Kruger, K. K. Kopecky, A. M. Aisen, D. R. Reinecke, G. A. Kruger, and W. L. Kiser, "Thermoacoustic ct with radio waves: a medical imaging paradigm," *Radiology*, vol. 211, pp. 275–278, Apr. 1999.

[2] G. Ku, B. D. Fornage, X. Jin, M. Xu, K. K. Hunt, and L. V. Wang, "Thermoacoustic and photoacoustic tomography of thick biological tissues toward breast imaging," *Technology in Cancer Research & Treatment*, vol. 4, pp. 1–7, Oct. 2005.

[3] C. G. A. Hoelen and F. F. M. de Mul, "Image reconstruction for photoacoustic scanning of tissue structures," *Applied Optics*, vol. 39, no. 31, pp. 5872–5883, 2000.

[4] J. Li, P. Stoica, and Z. Wang, "On robust Capon beamforming and diagonal loading," *IEEE Transactions on Signal Processing*, vol. 51, pp. 1702–1715, July 2003.

[5] T. Szabo, *Diagnostic Ultrasound Imaging: Inside Out*. Academic Press, Sept. 2004.

[6] Y. Xu and L. V. Wang, "Effects of acoustic heterogeneity in breast thermoacoustic tomography," *IEEE. Trans. Ultrason., Ferroelect. Freq. Contr.*, vol. 50, pp. 1134–1146, Sep. 2003.

[7] Q. Zhu and B. D. Steinberg, "Wavefront amplitude distribution in the female breast," *J. Acoust. Soc. Am.*, vol. 96, pp. 1–9, Jul. 1994.

[8] Y. Xie, B. Guo, L. Xu, J. Li, and P. Stoica, "Multi-static adaptive microwave imaging for early breast cancer detection," *39th ASILOMAR Conference on Signals, Systems and Computers*, pp. 285–289, Pacific Grove, CA, October 2005.

[9] M. Xu and L. V. Wang, "Time-domain reconstruction for thermoacoustic tomography in a spherical geometry," *IEEE Trans. Med. Imag.*, vol. 21, pp. 814–822, Jul. 2002.